Identification and characterization of human retinal stem cells capable of retinal regeneration

Jianzhong Su

sujz@wmu.edu.cn

Wenzhou Medical University https://orcid.org/0000-0003-1054-6042

Hui Liu

Laboratory of Stem Cell & Retinal Regeneration, Institute of Stem Cell Research; Division of Ophthalmic Genetics, The Eye Hospital, Wenzhou Medical University https://orcid.org/0000-0003-0444-5579

Yunlong Ma

Eye Hospital, Wenzhou Medical University

Na Gao

Eye Hospital, Wenzhou Medical University

Yijun Zhou

Eye Hospital, Wenzhou Medical University

gen Li

Qunyan Zhu

Wenzhou Institute, University of Chinese Academy of Sciences

Xiaoyu Liu

Wenzhou Medical University

Shasha Li

Oujiang Laboratory

Chunyu Deng

Wenzhou Medical University

Cheng Chen

Wenzhou Medical University

Yuhe Yang

Wenzhou Medical University

Qing Ren

Wenzhou Medical University

Huijuan Hu

Wenzhou Medical University

Yaoyao Cai

The First Affiliated Hospital of Wenzhou Medical University

Ming Chen

Wenzhou Medical University

Yuanchao Xue

Institute of Biophysics https://orcid.org/0000-0002-8113-2333

Kang Zhang

Macau University of Science and Technology https://orcid.org/0000-0002-4549-1697

Jia Qu

Eye Hospital, Wenzhou Medical University

Article

Keywords: human retinal stem cells, ciliary margin zone, retinal organoids, regeneration, multi-omic analysis, spatial transcriptomics

Posted Date: December 15th, 2023

DOI: https://doi.org/10.21203/rs.3.rs-3714208/v1

Additional Declarations: There is **NO** Competing Interest.

Abstract

Human retinal stem cells hold great promise in regenerative medicine, yet their existence and characteristics remain elusive. Here, we preformed single-cell multi-omics and spatial transcriptomics of human fetal retinas and uncovered a novel cell subpopulation, human neural retinal stem-like cells (hNRSCs), distinct from RPE stem-like cell and traditional retinal progenitor cells. These hNRSCs reside in the peripheral retina within the ciliary marginal zone, exhibiting substantial self-renewal and differentiation potential. We conducted single-cell and spatial transcriptomic analysis of human retinal organoids (hROs), and revealed hROs have remarkable similar hNRSCs consistent with fetal retina, capable of regenerating all retinal cells. Furthermore, we identified crucial transcription factors, notably *MECOM*, governing hNRSC commitment to neural retinogenesis and regulating hROs regeneration. Transplanting hRO-derived hNRSCs into the rd10 mouse of rapid retinal degeneration significantly repairs the degenerated retina and restores visual function. Together, our work identifies and characterizes a unique category of retinal stem cells from human retinas, underscoring their regenerative potential and promise for transplantation therapy.

Introduction

Retinal degeneration (RD) is currently one of the leading causes of blindness globally, encompassing conditions such as retinitis pigmentosa, macular degeneration, and congenital retinal dystrophies[1]. The primary pathological changes involve the irreversible degeneration of neural retina (NR) and/or retinal pigment epithelium (RPE) cells, ultimately resulting in permanent loss of visual function[1,2]. Current treatments primarily focus on alleviating the degeneration of NR cells and protecting remaining NR cells. There is still a lack of effective therapies aimed at promoting the regeneration of NR cells[3]. Stem cell-mediated retinal regeneration presents remarkable prospects for developing strategies to treat RD diseases[3,4]. However, the key challenge lies in the lack of optimal donor cells with NR regenerative potential. Retinal stem cells (RSCs), known for their unique ability to regenerate new NR cells, are considered the most direct and effective stem cells for treating RD diseases[5]. Nevertheless, over the last two decades, the existence and nature of RSCs in the human retina has been the subject of ongoing debate.

Lower vertebrates, such as zebrafish and amphibians possess an extraordinary ability to regenerate the retina owing to a specialized circular stem cell region at the interface between the NR and RPE, known as ciliary marginal zone (CMZ)[6–9]. Within the CMZ, there are RSCs and RPE stem cells that comprise a bipartite niche[10,11]. In contrast to classical retinal progenitor cells (RPCs) with only limited proliferation potential, RSCs are a unique population of cells with self-renewing and pluripotent capabilities, rendering them able to undergo unlimited cell divisions[8,11–13]. Throughout their entire lifespan, RSCs continuously generate new NR cells, which can rapidly proliferate and differentiate to repair the damaged retina[14–17].

The presence of RSCs in the retina of higher vertebrates is still uncertain[4,16,18,19]. Coles et al. suggested that RSCs could be found within the pigmented ciliary epithelium of both mouse and human CMZs[20–22]. These pigment cells were identified to be capable of forming clonal spheres through proliferation and differentiating into specific retinal cell types *in vitro*, implying the presence of RSCs with regenerative potential in the CMZ of higher vertebrates. However, contradictory to these findings, subsequent studies raised doubts that these proliferating pigment cells within the CMZ lacked the capability to differentiate into NR cells *in vitro*[4,23,24]. Instead, these cells appeared more akin to progenitors of the RPE lineage. More recently, multiple lines of evidence have indicated that stem like cells in the mouse CMZ could contribute to neural retinogenesis and the formation and function of binocular circuits[7,18,25]. To date, the presence and characteristics of RSCs within the human CMZ remain largely unknown due to the intricate nature of the retina and technological limitations.

Fortunately, groundbreaking technologies in single-cell and spatial transcriptomics sequencing have not only enabled the discovery of rare cell populations and precise cell locations but also offered valuable insights into developmental processes and cell differentiation pathways[26–30]. On the other hand, the development of human retinal organoids (hROs) has opened new avenues for investigating human retinal development and regeneration[31–33]. Our previous studies, as well as others, have demonstrated the potential of hROs in providing invaluable insights into the complexities of human retinal biology[34,35]. These hROs, derived from human pluripotent stem cells (hPSCs), faithfully emulate the structure and functionality of the *in vivo* retina, and replicate early retinal development[32,34,36]. Notably, prior investigations have observed CMZ-like structures within hROs[37,38]. Therefore, the combined utilization of single-cell approaches and hROs holds great promise in advancing our understanding of the human stem cell population residing in the CMZ of the retina.

In this study, by analyzing the transcriptomes and chromatin accessibility profiles at the single-cell level, we identified two distinct subpopulations of stem-like cells in the human fetal retina: human neural retina stem-like cells (hNRSCs) and RPE stem-like cells, which serve as the origins of two differentiation lineages for NR and RPE. The single-cell spatial transcriptomic data further reveal that these two stem cell populations exhibit discrete spatial locations within the CMZ. Importantly, hNRSCs exhibit significant distinctions from traditional RPCs and demonstrate heightened self-renewal abilities. In addition, we revealed the presence of a population of hNRSCs in the CMZ-like structure of hROs, which share a high degree of similarity with the native hNRSCs in fetal retina. Leveraging the hRO model, we demonstrated that hNRSCs could mediate neural retinal regeneration and characterize the dynamic changes in cells and molecules during regeneration. Moreover, hROs serve as an optimal stem cell reservoir, providing a substantial quantity of functional hNRSCs. Transplanting these hNRSCs into RD mouse models significantly preserves the retinal structure and improves visual function. Overall, this study uncovers hNRSCs in the CMZ of both fetal retinas and hROs, highlighting their regenerative functions and the potential application in transplantation therapy.

Results

Multi-omics of single cell unraveling the existence of hNRSCs in the CMZ of fetal retinas

To unravel the cellular heterogeneity and identify distinct cell types within the CMZ of human fetal retina, we utilized single-nucleus multi-omics sequencing (snATAC&GEX-Seq, 10x Genomics) to access gene expression and chromatin accessibility (ATAC) information for individual cells from both the CMZ and NR regions in 21-week fetal retinas (n = 4, Fig. 1a). Analysis of gene expression and chromatin accessibility in combination enabled us to uncover specific retinal cell types in CMZ and NR (Fig. 1b,c and Extended Data Fig. 1a). After stringently filtering, we obtained 16,540 high-qualified cells, including 7,562 cells from CMZ and 8,978 cells from NR (Extended Data Fig. 1b-d). By performing multimodal clustering based on both gene expression and chromatin accessibility data, 11 main cell clusters (C1-C11) were identified in the CMZ and control NR regions (Fig. 1c). Among them, we successfully annotated nine retinal cell types (C3-C11) based on the well-known marker genes, including RPCs, RPE, photoreceptor cell precursors (PC precursors), Müller glial cells (MCs), photoreceptor cells (PCs), amacrine cells (ACs), horizontal cells (HCs), bipolar cells (BCs), and retinal ganglion cells (RGCs) (Fig. 1d and Extended Data Fig. 2a,b).

Importantly, we identified two novel clusters, C1 and C2, displaying distinct expression patterns within the CMZ, characterized by the presence of several remarkable stemness-related genes (Fig. 1d and Extended Data Fig. 1b-d). The C1 cluster (denoted as Stem1) is specifically characterized by high expression levels of a subset of stemness-related genes, such as *MECOM*, *COL9A1*, *RELN* and *PCDH7* (Fig. 1d and Extended Data Fig. 2a,b), which are commonly recognized as markers or key regulators for adult stem cells[39–45]. Additionally, Stem1 cells are rich in CMZ marker genes, notably *ZIC1*, alongside critical genes such as *CPAMD8*, *MEIS1*and *TGFβ2* (Fig. 1d), which are likely to play significant roles in early retinal development[27,42,46,47]. On the other hand, the C2 cluster (denoted as Stem2) exhibits dual expression of stemness-related genes, such as *GJA1*, *PCDH7*, and *RELN*, alongside RPE development-associated genes, including *SLC6A15*, *MITF*, and *PMEL*[48]. Moreover, lacking expression of the mature RPE markers *CD96* and *BEST1* within this cluster, it suggests that these cells likely express the cellular features of early-stage RPE (Fig. 1d)[49]. Functional enrichment analysis further showed that these up-regulated genes in Stem1 were significantly enriched in biological processes relevant to stemness and neural retinogenesis, including stem cell division, stem cell proliferation, neural precursor cell proliferation, and photoreceptor cell differentiation (Extended Data Fig. 3a). While the up-regulated genes in Stem2 showed significant enrichments in RPE development-related biological processes, including pigmentation, epithelial cell proliferation, and morphogenesis of an epithelium (Extended Data Fig. 3b). Together, our results demonstrate that the Stem1 cluster exhibits characteristics of neural retinal stem cells may represent putative human neural retinal stem-like cells (named as hNRSCs), while the Stem2 cluster shows features of progenitors of RPE may represent putative RPE stem-like cells (named as RPE stem-like cells).

Furthermore, we performed an analysis using scVelo[50] to predict the developmental trajectories of the cell types based on RNA splicing events (Fig. 1e). We found that hNRSCs (Stem1) can transition to RPCs and further differentiate into PC precursors and PCs. As expected, PRE stem-like cells (Stem2) can

differentiate into PRE cells. To further validate these cell lineage transitions, we applied Monocle3[51], an unsupervised algorithm, to order the whole-transcriptome profiles of single cells. These results supported the proposed NR lineage transition which is from hNRSCs to RPCs, PC precursors, and PCs (Lineage 1), as well as the RPE lineage which is transition from RPE stem-like cells to RPE cells (Lineage 2) (Fig. 1f and Extended Data Fig. 3c). Meanwhile, we also used Monocle3 to order the chromatin accessibility profiles of single cells and observed a similar developmental trajectory (Extended Data Fig. 3d). Consistent evidence for the lineage transitions was also validated by an orthogonal method of partition-based graph abstraction (PAGA) (Extended Data Fig. 3e)[52]. Moreover, we utilized cytoTRACE [53] to assess the stemness of the four early cell types in lineage 1, namely hNRSCs, RPCs, PC precursors, and PCs (Fig. 1g). Results demonstrated that hNRSCs exhibited the highest stemness scores compared to others (Fig. 1g). An entropy-based inference method[54] also confirmed the highest stemness of hNRSCs in lineage 1 (Extended Data Fig. 3f).

To identify critical transcription factors (TFs) that are involved in the commitment of hNRSCs in neural retinogenesis, we used the Pando[55] to conduct an in-depth analysis of highly active TFs and their downstream regulatory genes via integrating fetal retinal single-cell transcriptomic and ATAC data (Fig. 1h and Extended Data Fig. 4a). By visualizing a UMAP embedding, we found that the critical TFs (such as *MECOM* and *TBX20*) tracked transitions from hNRSCs to RPCs-PC precursors-PCs axis (Fig. 1h right upper panel and Extended Data Fig. 4b). A total of 272 genes targeted by nine TFs, including *MECOM*, *TBX20*, *THRB*, and *ESRRG*, were identified to be significantly specific to hNRSCs (Extended Data Fig. 4c). Functional enrichment analysis showed that these hNRSC-specific TFs and their targeted genes were significantly enriched in biological processes related to neurogenesis and retinal differentiation (Fig. 1h right lower panel and Extended Data Fig. 4d), including synapse organization, axon development and positive regulation of neurogenesis. Based on an independent method of SCENIC[56], we consistently found that these specific TFs exhibited high regulon activities within hNRSCs (Extended Data Fig. 4e,f). Together, our results demonstrate that two stem-like cell types in fetal CMZ contribute to two distinct differentiation transitions of NR lineage and RPE lineage.

hNRSCs reside in the non-pigmented CMZ with high self-renewal and differentiation potential for retinal cell lineage

To determine the accurate spatial location of hNRSCs and RPE stem-like cells within the human CMZ, we collected a fetal eye sample from a spontaneous abortion that occurred at 19 weeks of gestation. We used high-definition and large-field spatial enhanced resolution omics sequencing (Stereo-seq) to generate spatial transcriptomic data from section that covered the globe of the eye (Extended Data Fig. 5a,b). By performing the spatially constrained clustering analysis, we identified 57 distinct cell clusters (Extended Data Fig. 5c, c1-2). Of them, cluster-43 is found to reside in the CMZ region. To enhance the cell type annotation within the CMZ region, we independently re-clustered this region and identified three distinct sub-clusters (Extended Data Fig. 5c, c3). With reference to the cell markers from

single-cell transcriptomic data, we have successfully identified the precise spatial localization of the hNRSC cluster. This cluster, which is characterized by the expression of markers such as *CPAMD8*, *MECOM* and *COL9A1*, is located in the peripheral retina within the CMZ (Fig. 2a and Extended Data Fig. 5c, c3). Adjacent to the hNRSC cluster and connected to the RPE layer, we successfully identified a cell cluster as RPE stem-like cells, which express *GJA1* and *TFPI2* (Fig. 2a and Extended Data Fig. 5c, c3). Finally, leveraging the different expression genes and established cell marker genes, we annotated 23 other cell types located in specific regions throughout the eye, including RPCs, PCs, RGCs, BCs, ACs, HCs, RPE, and glial cells in the retina region, fibroblasts and endothelial cells in the sclera and choroid regions; and epithelial cells and stromal cells in the regions of the cornea and lens (Fig. 2a and Extended Data Fig. 5d, e). To further verify the lineage transition of cells in CMZ, we employed cell lineage and pseudotime inference to analyze the progression of hNRSC, RPCs, and PCs. The result consistently supports the putative lineage transition along the hNRSCs-RPCs-PCs axis, which is also characterized by spatial proximity and continuity in growth trajectory (Fig. 2a). Our spatial transcriptomic data illuminate the precise spatial localization of hNRSCs and RPE stem-like cells within the human CMZ.

To further investigate hNRSCs within the human CMZ, we collected additional fetal retinas (n = 10) from spontaneous abortions that occurred between 16–22 weeks of gestation. Employing Hematoxylin and Eosin (H&E) staining, we observed a dual-layer structure in the CMZ of fetal retina, with one layer being the non-pigmented CMZ region connected to the NR, and another layer being the pigmented CMZ region, distinguished by its prominent pigmentation and connected to the RPE (Fig. 2b and Extended Data Fig. 6a). We then conducted immunofluorescence staining to examine the spatial expression patterns of marker genes associated with hNRSCs and RPE stem-like cells. In accordance with the spatial transcriptomic data, the results revealed that hNRSC markers, such as MECOM, CPAMD8, and COL9A1, were predominantly localized in the peripheral NR and non-pigmented CMZ (Fig. 2c). Conversely, RPE stem-like cells, identified by positive staining for GJA1 (Cx43), were mainly distributed in the pigmented CMZ connected to the RPE layer (Fig. 2c). As expected, other retinal cell markers such as Brn3a, RCVRN and PROX1, were primarily observed in the central region of the NR (Fig. 2c and Extended Data Fig. 6b). Therefore, these results further confirm that hNRSCs and RPE stem-like cells are resided in separate locations within the CMZ region.

Next, we performed a clonal sphere-forming and induced differentiation assay to evaluate the self-renewal and differentiation potential of hNRSCs *in vitro* under serum-free conditions. By staining with the surface marker CPAMD8 and sorting by flow cytometry (FACS), we successfully isolated CPAMD8-positive ($CPAMD8^+$) hNRSCs from the non-pigmented CMZ. These hNRSCs were then subjected to the clonal sphere assay in a serum-free environment, with cells isolated from the NR region (NR cells) serving as the control (Fig. 2d and Extended Data Fig. 6c). It was shown that CMZ cells, particularly the $CPAMD8^+$ hNRSCs, demonstrate a significantly enhanced ability to form clonal spheres compared to NR cells (Fig. 2d,e). As expected, we found that these hNRSC spheres expressed marker genes like MECOM and CPAMD8, and exhibited positive EdU staining, supporting the proliferative potential of hNRSCs (Fig. 2f). After inducing the differentiation of these hNRSC spheres under specific conditions for three weeks, we

analyzed the gene expression profiles of various retinal cell types based on RNA-Seq data. As shown in Fig. 2g, genes enriched in hNRSCs exhibited significant down-regulation in the cells differentiated for 21 days. In contrast, the differentiated cells displayed a remarkable up-regulation of genes associated with various types of retinal cells (Fig. 2g and Supplementary Table 1). Consistent with these findings, immunostaining analysis revealed that hNRSCs possess the capability to differentiate into major retinal cell types, including RPCs ($PAX6^+/SOX2^+$), RGCs ($PAX6^+/SOX2^-$ or $Brn3a^+$), HCs/ACs ($PROX1^+$), PC precursors (CRX^+), PCs (NRL^+ or $ARR3^+$) and BCs ($CHX10^+$) (Fig. 2h and Extended Data Fig. 6d). These results suggest that hNRSCs possess both the characteristics of self-renewal and the potential for differentiation into all retinal cells. Furthermore, FACS-purified $GJA1^+$ ($Cx43^+$) pigmented cells (RPE stem-like cells) from the pigmented CMZ region also possess the ability to form clonal spheres (Extended Data Fig. 6e). However, these spheres exhibited noticeable pigmentation and ultimately lacked the inclination to differentiate into other retinal cells (Extended Data Fig. 6e). Together, we precisely localized the distribution of hNRSCs in the CMZ region of human fetal retina, and confirmed the stemness and differentiation potential of hNRSCs.

CMZ of hROs mediates the neural retina regeneration

hROs can closely mimic the *in vivo* retina[34]. During the cultivation of hROs, we observed that approximately 80% of the hROs developed CMZ-like structures, which were located in a specific hinge zone between the NR and RPE and displayed a distinct elongated wedge-shaped morphology, reminiscent of a specialized stem cell niche (Fig. 3a,b and Extended Data Fig. 7a,b). Remarkably, hROs with CMZ-like structures showed significantly enhanced survival rates and overall viability compared to those lacking this anatomical feature (Fig. 3c). Additionally, certain hROs exhibited a root-like structure, which had simultaneous proliferation of multiple NR connecting to only one CMZ (Extended Data Fig. 7c). These observations collectively suggested that the CMZ-like structures of hROs may possess regenerative capability for the retina.

To investigate the regenerative potential mediated by cells in the CMZ region of hROs, we developed a *VSX2* (serving as an RPC or BC marker and expressed in NR region)-tdTomato reporter human embryonic stem cells (hESCs) with normal karyotype, pluripotency, and differentiation capacity by the insertion of the 2A-tdTomato sequence in-frame into the exon 5 of *VSX2* gene (Extended Data Fig. 7d-g). This strategic insertion, positioned before the stop codon, ensures the tracing of NR regenerative lineage through tdTomato expression (Fig. 3d). By inducing the formation of hROs, this modified hESC line enabled the visualization of tdTomato-positive RPCs, which was primarily located within the central NR region that clearly demarcated the NR and CMZ interface after 75 days of differentiation (Fig. 3d,e). To further examine the dynamic changes during retinal regeneration and repair mediated by CMZ, we established a culture system that allows real-time monitoring of the process. Briefly, mature hROs beyond day 75 were selected, and the NR region labeled with *VSX2*-tdTomato was surgically excised while the CMZ was preserved for subsequent cultivation (Fig. 3f). Imaging results illustrated the progressive regeneration of the fluorescently labeled NR at the precise location of the excision (Fig. 3f). Remarkably,

the regenerated retina exhibited indistinguishable morphological structure compared to normally developed hROs (Fig. 3f). In contrast, the control groups containing only NR or RPE displayed no discernible retinal regeneration (Extended Data Fig. 7h,i).

Next, we conducted a one-day EdU exposure to label actively dividing cells within the CMZ after excising the NR at the developmental stage day 75. This enabled us to trace the de novo generation of the NR at its periphery during regeneration (Fig. 3g). Results revealed that a significant number of CMZ cells continued to undergo mitosis and were incorporated by EdU. Additionally, it was observed that the labeled dividing cells from the CMZ expanded towards the central region of the regenerating NR as the regeneration process unfolded (Fig. 3g). At the day 24 of the regeneration, these dividing cells were uniformly distributed throughout the central regenerating retina. Through the comparative analysis of bulk RNA transcriptomic data based on five time points of retinal regeneration and normal development, we found that all cell types observed in the normal developing retina could be regenerated during the retinal regeneration process (Fig. 3h and Extended Data Fig. 7j; Supplementary Table 2,3). Notably, principal component analysis of these transcriptomic data revealed a similar pattern of transcriptional changes in both the processes of regeneration and normal development (Fig. 3i), suggesting that NR regeneration may recapitulate the process of NR development. Furthermore, immunostaining of organoid sections provided additional verification that the molecular and morphogenetic characteristics of the regenerated hROs were consistent with those of the normal developed hROs (Fig. 3j)[34]. Overall, our findings highlight the critical roles of hRO-derived CMZ-like structures in driving NR regeneration, providing previously unrecognized functional insights in understanding of retinal regeneration mechanisms.

hNRSCs within the CMZ of hROs have consistent characteristics with fetal retina

Considering the regenerative function of CMZ-like structures within hROs, we speculated that these structures might contain hNRSCs resembling those present in the fetal retinal CMZ. Consequently, we proceeded to collect hROs at the developmental stage of 75 days for single-nucleus RNA sequencing (snRNA-seq, 10x Genomics) and obtained 7,227 high-qualified cells analogous to fetal single-cell analysis. We clustered these cells and annotated them into 10 cell types using well-known marker genes (Fig. 4a and Extended Data Fig. 8a,b). To compare the similarity of cell types between the hROs and fetal retinas, we combined the single-cell transcriptomic data from both the hROs and the fetal retinas, in reference to a previous study[57]. The results showed a significantly high overlap between both datasets in term of cellular compositions ($r = 0.93$, $P = 1.27\times10^{-4}$, Fig. 4a and Extended Data Fig. 8c-e). Moreover, we quantitatively measured the closeness between hROs and fetal retina via calculating the Jaccard similarity index (JSI) of highly specifically expressed marker genes in each cell type among both single-cell datasets. A high similarity of marker genes across cell types was observed between the hROs and fetal retina (Fig. 4b). Especially, we found that hNRSC-specific marker genes showed a higher consistence between the hROs and fetal retina (JSI = 0.26, Fig. 4b). Functional enrichment analysis using hNRSC-

specific marker genes demonstrated that there were several significantly enriched biological processes relevant to neurogenesis and cell development shared by both the hROs and fetal retina (Extended Data Fig. 8f). Together, these results affirmed that hNRSCs within hROs closely resemble those in the fetus context.

To accurately investigate the spatial distribution of hNRSCs within the CMZ-like structures of hROs, we employed spatial transcriptomic (ST, 10x Genomics) sequencing on 75-day-old hROs. Considering the tiny size of hROs, we prepared H&E sections of four hROs to assess the spatial organization by ST sequencing (Fig. 4c, left panel). Based on the unbiased clustering and spot features, we classified the spots into 6 clusters, namely RGCs/RPCs, RPCs/PC_precursors/MCs, RPE/RPE stem-like cells, hNRSCs, RPCs/PCs/ACs_HCs/BCs/MCs and RPCs/PCs (Fig. 4c, right panel), annotating by using well-defined marker genes (Fig. 4d). Based on the ST sequencing analysis, we consistently found that retinal cell types were primarily situated within the NR region of hROs, distributing from outmost PCs to intermediate RPCs to inner HCs, ACs, and BCs, while RPE stem-like cells and RPEs were mainly located on the opposite end of the NR region (Fig. 4c). Notably, hNRSCs occupied the hinged CMZ region between the NR and RPE, suggesting that the hROs can closely mimic the cellular distribution pattern in the human fetal retina (Fig. 4c and Fig. 2c). Moreover, we leveraged the top 20 specifically expressed genes of hNRSCs in snRNA-seq data in the same developmental stage to score the spots in each ST cluster, and found that the hinge region obtained the highest hNRSCs-derived signature scores, providing orthogonal evidence to support hNRSCs locate in the hinge region (Fig. 4e). Next, temporal analysis was performed to verify the developmental trajectory using stlearn[58]. The predicted lineage transition of these spots along pseudotimes revealed that the hNRSCs of hROs possess inherent retinal differentiation lineage, which is consistent with the lineage transitions found in fetal CMZ (Fig. 4f). Subsequently, immunofluorescence staining further confirmed the specific localization of hNRSCs within this hinge region of the CMZ, which is situated precisely between the NR and the RPE (Fig. 4g and Extended Data Fig. 9a). This localization of hNRSCs within the CMZ suggested that the hROs contain a niche that harbors cells with characteristics resembling those of hNRSCs and RPE stem-like cells (Extended Data Fig. 9b) identified in the developing fetal retinas. Additionally, we isolated hNRSCs from hROs and performed clonal sphere assays. It was shown that hNRSCs have a significantly greater capacity for clonal sphere formation in comparison to normal NR cells (Extended Data Fig. 9c,d). These results further support the presence and spatial distribution of hNRSCs within the CMZ-like structures of hROs. In conclusion, hROs exhibit a remarkable ability to faithfully recreate hNRSCs presented in the human fetal stage, providing alternative and abundant material for investigating the cellular and molecular characteristics of hNRSCs, and exploring their roles in retinal regeneration and repair.

Cellular and molecular dynamics underlying neural retina regeneration

To unravel the intricate cellular and molecular dynamics underlying hNRSC-driven retinal regeneration, we conducted snRNA-seq analysis of hROs across five time points (Regenerative stage day 0, 5, 10, 20, and 40) during the regeneration process (Fig. 5a). A total of 19,002 cells were available for downstream

analyses after quality control. By subjecting these cells into UMAP based on highly variable genes, we clustered these cells and assigned well-known marker genes to annotate these clusters (Fig. 5b and Extended Data Fig. 10a). Consistent with the fetal retina results, our analysis identified 10 major cell types within the regenerating hROs, including hNRSCs, RPCs, PC precursors, and PCs of lineage 1, as well as RPE stem-like cells and RPE of lineage 2 (Extended Data Fig. 10b,c).

To further validate the above lineage transitions of identified in fetal retina, we leveraged Monocle3 to predict cell developmental trajectory based on the whole single-cell transcriptomic profile of regenerating hROs. As expected, these results offered supportive evidence for the postulated lineage transition that NR cells was along the axis encompassing hNRSCs-RPCs-PC precursors-PCs (lineage 1, Fig. 5c), while the lineage transition of RPE cells was along the axis of RPE stem-like cells to RPE cells (lineage 2, Fig. 5c). The pesudotimes of cells in hNRSCs were remarkably earlier than those of the other three cell types in lineage 1 (Fig. 5d and Extended Data Fig. 10d). To explore the dynamics of four cell types in lineage 1 during the regeneration, we assessed the ratio of cell proportion of each cell type in the four regenerative time points (i.e., day 5, day 10, day 20, and day 40) compared to the initial time point (day 0). An increasing trend was found in hNRSCs from day 0 to day 20 and the cell ratio turned to reduce from day 20 to day 40, while an opposite trend observed in RPCs that was decreased from day 0 to day 20 and became increase from day 20 to day 40 (Fig. 5e). One population was PCs showing similar patterns with RPCs. The other population of PC precursors was observed to be increased from day 0 to day 40. These results indicate that hNRSCs were stimulated in response to the surgical excision, and RPCs likely were recruited to participate in the regenerative process for increasing the cell composition of other cell types. By in-depth analysis of Monocle results across these time points, we consistently found that the pesudotimes of cells are positively correlated with the regenerative process (Fig. 5f).

Moreover, we utilized the method cytoTRACE to assess the cell differentiation dynamics in all cell types across these five regenerative time points. We observed an initial augmentation in cellular stemness after the surgical excision of NR region, followed by a decline from day 5 to day 40 (Fig. 5g). Using an orthogonal method of Stem_ID, we validated a consistent trend that cells in day 5 yielded the highest stemness compared to other time points (Extended Data Fig. 10e). These results indicate that the stem-like cells we identified at day 5 were activated for proliferation and differentiation, aligning with active stem cell activities in previous studies[28]. To discover the molecular features of stem cells involved in this activation process, we conducted a differential gene expression analysis to pinpoint potential genes which are pivotal in neural retinogenesis. In comparison with the initial time point (day 0), we identified 221 significantly up-regulated genes in hNRSCs at day 5 (FDR $\leq$ 0.05, log2 FC $\geq$ 2, Fig. 5h), including *MECOM*, *TBX20*, *COL9A1*, *CPAMD8*, *NFIA* and *MEIS1*, which are either specifically expressed in hNRSCs or associated with early retinal development. GO enrichment analysis showed that these up-regulated genes were prominently enriched in biological processes related to chromatin organization, cell cycle, and stem cell proliferation (FDR < 0.05, Extended Data Fig. 11a). Among these up-regulated genes, the TF of *MECOM* exhibited an increased activity after the regeneration initiation (Fig. 5i), reminiscing that *MECOM* is a hub hNRSC-specific TF targeted with several functional genes in above Pando-based network

analysis using fetal retinal single-cell transcriptomic and ATAC-seq data (Fig. 1h, Extended Data Fig. 4c and 12a). Consistent with fetal retina results, we also found that *MECOM* showed a highly specific regulon activity to hNRSCs in this hRO regeneration dataset (Extended Data Fig. 12b). Based on Monocle-predicted pesudotimes from both hRO regeneration and fetal retina datasets, *MECOM* and its targeted genes were detected to be primarily expressed in the earlier stage of transition trajectory (Extended Data Fig. 12c). By calculating the activity score of *MECOM*-targeted genes using the *AddModuleScore* function in Seurat[59], we observed that these targeted genes were mainly activated in the cell types of lineage 1 (Extended Data Fig. 12d). Functionally, these targeted genes were remarkably enriched in biological processes relevant to sensory organ development and visual perception (FDR < 0.05, Extended Data Fig. 12d).

To further investigate the functional roles, we then employed CRISPR/Cas9 lentiviral-mediated approach to knockdown *MECOM* of hNRSCs within hROs at development stage day 75. Following 120 h of viral infection, a successful silencing efficiency of over 80% was achieved for the targeted genes (Fig. 5j and Extended Data Fig. 13a). Subsequently, regeneration experiments were conducted on the genetically modified hROs. Results showed that MECOM knockdown led to a comparatively pronounced inhibition of hRO regeneration (Fig. 5k). In comparison to the negative control group, *MECOM* knockdown resulted in a significant reduction in the size of regenerated hROs, indicating an impaired regenerative capacity (Fig. 5k,l). Additionally, the structural integrity of the NR was compromised, displaying abnormalities attributable to the *MECOM* knockdown (Extended Data Fig. 13a,b and Fig. 3j). Furthermore, the development of various retinal cell types was also hindered (Extended Data Fig. 13b and Fig. 3j). Together, our results provide substantial evidence to support that hNRSCs have the proliferative potential to cover the wound area and differentiate into retinal cells to promote regeneration. We further highlight a TF MECOM that has a critical role in governing retinal regeneration and emphasize its contribution to the proper differentiation of retinal cells within hROs.

Transplanting hRO-derived hNRSCs for treating retinal degeneration in mice

Given the regenerative potential of hNRSCs observed *in vitro*, we further investigated whether these cells purified from the CMZ of hROs are suitable for subretinal transplantation therapy in mouse models with RD disease (Fig. 6a). Safety is a critical consideration in stem cell transplantation therapy[60]. We initially focused on conducting a comprehensive safety assessment of hNRSCs within the context of transplantation therapy. Healthy hROs derived from ESRG Pr-tdTomato reporter H9 hESCs (where ESRG serves as a known marker for hPSCs)[61,62] were selected beyond day 75 (Extended Data Fig. 14a,b). After surgically removing the NR region and allowing it to regenerate for 5 days, the CMZ was dissociated into single cells for flow cytometry analysis. The findings indicated that the proportion of potentially tumorigenic hPSCs in the CMZ was extremely rare, implying that the transplantation of these cells would likely pose minimal risk of tumorigenicity (Extended Data Fig. 14c). Additionally, CPAMD8^{+} hNRSCs were isolated using FACS from the CMZ of the 5-day-regenerated hROs, which were exclusively labeled with tdTomato, and then transplanted into the subretinal space of 4-week-old BALB/c Nude mice (Extended

Data Fig. 14d). Two months after transplantation, no intraocular tumors were observed in the eyes that received hNRSCs. In contrast, among the mice transplanted with H9 hESCs (labeled with tdTomato), eight out of ten exhibited visible tumors within the eyes, providing additional evidence supporting the safety of hNRSC transplantation (Fig. 6b).

Next, we proceeded to evaluate the effectiveness of hNRSC transplantation therapy in rd10 mice, a well-established model of autosomal recessive retinitis pigmentosa. To ensure an abundant supply of functional hNRSCs, we specifically selected *VSX2*-tdTomato reporter hROs at the regenerative stage day 5, during which the cells exhibit relatively higher quantities and vitality (Fig. 5e,i). The regions corresponding to the NR and RPE were surgically removed. Afterward, the remaining CMZ was enzymatically dissociated into individual cells, and CPAMD8^{+} hNRSCs were isolated and then transplanted into the subretinal space of rd10 mice at postnatal weeks 2–3, when photoreceptor degeneration was in progress (Fig. 6a). Notably, 12 weeks after hNRSC transplantation, a substantial and well-organized population of *VSX2*-tdTomato-positive transplanted cells was observed in the outer aspect of the inner nuclear layer in eyes, suggesting that the transplanted hNRSCs survived and differentiated into the retinal cells (Fig. 6c). Further investigation also confirmed that there was a notable portion of transplanted cells exhibited photoreceptor characteristics, displaying robust expression of photoreceptor-specific markers such as RCVRN, CRX, and NRL (Fig. 6c,d). To monitor the survival and differentiation of cells at later stages post-transplantation, antibodies against the human-specific marker Ku80 (Ku86) were used. As expected, all transplanted cells co-expressed Ku80, confirming their donor origin (Fig. 6e and Extended Data Fig. 14e). 20 weeks after transplantation, a substantial number of Ku80^{+} cells were still alive and had differentiated and integrated (Fig. 6f,g and Extended Data Fig. 14f,g). Among them were mature photoreceptors in the outer nuclear layer expressing L/M-opsin or Rhodopsin (Fig. 6f and Extended Data Fig. 14f,g), and RGCs in the inner nuclear layer expressing RBPMS (Fig. 6g). Moreover, to assess the connectivity and integration between the transplanted cells and host cells, we also transplanted hNRSCs isolated from hROs solely labeled with tdTomato. After 20 weeks post-transplantation, tdTomato-positive engrafted cells displayed distinct synaptic terminals, as indicated by the presence of the rod ribbon-synapse protein ribeye (labeled by CTBP-2) and the presynaptic protein PSD95 (Fig. 6h,i). Importantly, these synaptic terminals formed connections with rod bipolar cells (identified by the bipolar marker PKC-α), which play a crucial role in transmitting light signals to the inner retinal layers (Fig. 6i).

To delve deeper into potential functional synaptic connectivity, scotopic flash electroretinography (fERG) was conducted on the transplanted rd10 mice to evaluate the efficacy of the treatment (Fig. 6j). The fERG analysis exhibited a notable elevation in the amplitude of b-waves in the eyes that underwent hNRSC transplantation, as compared to the control (sham-transplanted) groups, from 4 weeks to 20 weeks post-transplantation (Fig. 6j). Furthermore, visual acuity was assessed utilizing the optokinetic response (OKR) test, a more sensitive approach, from 4 weeks to 20 weeks after transplantation (Fig. 6k). In comparison to the control groups, the hNRSC-transplanted groups exhibited significant improvement and maintained stability at 4-, 8-, 12-, 16- and 20-weeks post-transplantation (Fig. 6k). Morphologically, we noted that

transplanted hNRSCs effectively protected photoreceptors from degeneration (Fig. 6c-g and Extended Data Fig. 14h). Importantly, the transplanted cells exhibited strong viability, persisting up to 24 weeks after transplantation, highlighting their potential to maintain long-term effectiveness in transplantation therapy (Extended Data Fig. 14i). In summary, these findings collectively suggest that transplanted hNRSCs not only survived and underwent differentiation into retinal cells but also integrated and formed connections with the host retinal cells in rd10 mice. These hRO-derived hNRSCs are a promising therapeutic cell source.

Discussion

Unveiling the existence of retinal stem cells within the CMZ of human retina and comprehending their characteristics and functions holds paramount importance for driving progress across fields such as retinal development and regenerative medicine. However, over the past two decades, the presence of stem cell types within the human retina remains elusive. In this study, we integrated single-cell multi-omics and spatial transcriptomics data to identify two stem cell subpopulations (hNRSCs and RPE stem-like cells) in the CMZ of the human fetal retina, which exhibit unique spatial locations, molecular features, and capabilities in terms of self-renewal and differentiation. Based on organoid technologies, we found that the hNRSCs in the CMZ of hROs closely resemble those found in the fetal retina and elucidated their roles in mediating retinal regeneration. Lastly, we successfully used hNRSCs derived from hROs for subretinal transplantation, and effectively treated mice with RD diseases.

In contrast to classical RPCs with limited proliferation potential, RSCs are a unique population of cells with stronger self-renewal and pluripotent capabilities, making them highly valuable for potential applications in regenerative medicine and the treatment of retinal diseases[63]. In lower vertebrates, RSCs originate from the CMZ of the peripheral retina. These cells have the remarkable capacity to generate all retinal cell types[10,64]. Additionally, the CMZ region of hatched chicks also contains RSCs[65]. In humans, particularly in fetal retinas, an identifiable CMZ structure exists. However, due to the complexity of retinas, the scarcity of stem cells, and the absence of well-defined markers, it has remained uncertain whether the CMZ region in fetal retinas harbors RSCs capable of regenerating retinal function. Single-cell multi-omics holds tremendous potential for discovering and analyzing previously unrecognized rare cells[30]. Here, we isolated the CMZ regions from human fetal retinas, performed region-specific single-cell multi-omic analysis, combined with spatial transcriptomic analysis and *in vitro* validation experiments. Ultimately, we successfully identified a unique neural retinal stem-like cell type, named hNRSCs, within the CMZ of the fetal retina. These cells are characterized by their distinctive spatial distributions, molecular profiles, and remarkable capacities in terms of self-renewal and differentiation. Earlier studies indicated that a group of pigmented RSCs were detected to be capable of forming cell spheres *in vitro* in the pigmented CMZ of mammals[20,21]. However, accumulating evidence suggests that these pigmented RSCs might only differentiate into RPE rather than neural retina[23,24]. Here, we have also identified another stem-like cell subpopulation in the pigmented CMZ of human, which not only express certain markers related to stemness but also possess early RPE lineage characteristics. And their spatial location resides near the

side of the RPE layer. Based on systematic genomic analyses and molecular experiments, we revealed that this cell subpopulation predisposes to develop into RPE and form pigmented cell spheres without the ability to differentiate into retinal cells *in vitro*. We define this cell population as RPE stem-like cells, which share similar characteristics with previously reported pigmented RSCs in earlier studies [21].

The fetal retinal CMZ contains hNRSCs, but ethical concerns, the scarcity of donors for fetal retinas, and notably, the limited quantity of hNRSCs severely restrict fundamental research into the characteristics and functions of hNRSCs, as well as research related to their clinical applications[66]. Although these hNRSCs can be isolated from the CMZ using FACS, challenges arise when attempting functional expansion after the loss of the CMZ microenvironment. Currently, the only practical approach for culturing these cells is in the form of clonal spheres. Nevertheless, there is still an issue of stemness loss during clonal passaging. We thus hypothesize that the CMZ microenvironment plays a critical role in maintaining the properties of hNRSCs. Future researches are warranted to focus on investigating the microenvironment within the CMZ region, potentially by adding key regulatory factors, to establish a stable cultivation system for hNRSCs, and eventually achieve substantial functional expansion *in vitro*. Fortunately, we have currently identified a more optimal cell source, in-dish hROs, which can continuously supply functional hNRSCs. Organoids have the capability to closely mimic the physiological structure and function of organs and are commonly referred to as in-dish organs[67]. In 2012, Nakano et al. pioneered the creation of hROs using hESCs, which accurately replicate early retinal development[31]. Leveraging this technique, we have previously succeeded in constructing hROs and retinoblastoma organoids to trace the origin of tumor cells using single-cell analysis[34,68]. Earlier study by Kuwahara et al. suggested the presence of CMZ-like structures in hROs[38]. In this study, we confirmed the existence of CMZ-like structures in hROs that resemble those found in fetal retinas. Additionally, we provided strong evidence that these CMZ-like structures actively support retinal regeneration within hROs. Most importantly, through employing single-cell and spatial transcriptomic analysis, we successfully identified hNRSCs within the CMZ-like structures of hROs. These hNRSCs exhibit cellular and molecular features highly akin to those found in the fetal retina. Remarkably, within the CMZ-like structures of hROs, there is a substantial population of highly active and functionally potent hNRSCs. This abundant supply provides an ideal foundation for investigating the role of hNRSCs in retinal regeneration and exploring their potential for transplantation-based therapies for RD diseases.

Based on single-cell multi-omics data from fetal retinas, we identified the core TF, *MECOM*, which exhibited high regulon activities in hNRSCs. Previous studies have indicated that *MECOM* serves as both a TF regulator and an epigenetic modifier, playing a crucial regulatory role in adult stem cell proliferation, differentiation, and embryonic development by modulating signaling pathways such as JNK and TGF-β[39,69,70]. For example, *MECOM* regulates downstream target genes to maintain the proliferation and homeostasis of hematopoietic stem cells and influences their fate determination[39,40,69]. Previous studies also suggested that *MECOM* may be involved in chromatin remodeling to regulate early retinogenesis[42]. In our research, we observed a significant up-regulation of *MECOM* expression and regulon activity during the initial stages of regeneration. Targeted genes of *MECOM* were primarily expressed in the early stage

of the transition trajectory and were mainly activated in cell types of lineages 1 (hNRSCs-RPCs-PC precursors-PCs axis). Using efficient gene editing techniques, we observed that the knockdown of *MECOM* in hNRSCs significantly inhibited retinal regeneration. The regenerated retina exhibited significant abnormalities in both external morphology and internal structure, indicating that *MECOM* plays a crucial regulatory role in the process of retinal regeneration and differentiation mediated by hNRSCs. Besides *MECOM*, we have identified other highly active TFs, including *TBX20*, *THRB*, and *NFIA* specific to hNRSCs. These TFs, along with their corresponding target genes, collectively form a complex co-regulatory network that is likely involved in directing the commitment of hNRSCs during retinogenesis. Enhancing the understanding of the regulatory mechanisms of these TFs in the future could potentially lead to advancements in acquiring high-quality hNRSCs, controlling their directed differentiation, and achieving *in vivo* regeneration.

Human retinal damage and associated diseases often lead to irreversible vision loss. Stem cell therapy has long been considered an effective treatment for such conditions[3,71]. In current reported researches on treating RD using stem cells, various seed cells have been tested, but each comes with its limitations[3,4,72]. Instead, hNRSCs offer a unique advantage, as they are capable of differentiating directly into retinal cells within the body's native microenvironment. Notably, hNRSCs exhibit high safety profiles and minimal tumorigenic potential. Moreover, their low immunogenicity, especially in autologous settings, serves as a safeguard against immune rejection. The use of hNRSCs in treating RD holds promise for enhanced specificity when compared to other stem cell types. Additionally, a significant challenge in cell transplantation therapy for RD is the insufficient activity and functionality of donor cells, leading to difficulties in adapting to the host environment, as well as hindered survival and differentiation post-transplantation. By utilizing these hNRSCs isolated from the regenerative environment, they are primed to adapt to the injury environment, being in an active and regenerative state, which makes them more likely to survive and differentiate when used for transplantation therapy. Indeed, we sorted hNRSCs from the hROs at the regenerative age of day 5 and transplanted them into the subretinal space of the rd10 mouse model. These transplanted hNRSCs were able to survive, differentiate into retinal cells, and these newly generated retinal cells could integrate and establish connections with host cells, leading to a partial improvement in visual function in the retinal degeneration mice. Collectively, hNRSCs derived from hROs emerge as a promising therapeutic cell source.

In conclusion, we have identified a novel population of hNRSCs located within the CMZ of both fetal retinas and hROs. These cells exhibit remarkable capabilities for self-renewal and differentiation into all types of retinal cells. We have comprehensively characterized their biological properties and molecular features, delving into the role of these hNRSCs in the process of retinal regeneration and repair. The significance of this research not only deepens our understanding of retinal biology but also holds immense potential for advancing therapeutic interventions in retinal degenerative diseases.

Methods

Mice

rd10 (Pde6b^{rd10}, C57BL/6J genetic background) mice were purchased from Jackson Laboratory. BALB/c-Nude mice were purchased from Charles River. All mice used in this research were housed under specific pathogen-free conditions. All procedures conducted on these animals were in compliance with ethical animal license protocols and received approval from the Laboratory Animal Ethics Committee of Wenzhou Medical University (Research License wydw2023-0223).

Cell lines

H9 hESCs (WiCell) and their derivatives were cultured in accordance with established procedures[68]. In brief, the cells were grown on plates coated with Matrigel (Corning, 356231) in TeSR-E8 medium (Stem cell Technologies, 5990) at 37°C within a 5% CO_2 incubator. The culture medium was refreshed daily, and cell morphology was observed using an inverted fluorescence microscope (ZEISS). Passaging of cells was performed routinely every 4–5 days using 0.5 μM EDTA solutions (Gibco, AM9261), and they were transferred to Matrigel-coated plates in TeSR-E8 medium supplemented with 10 μM Y-27632 (Selleck, S1049) to uphold their pluripotent state. HEK-293 cells were cultured in DMEM (Dulbecco's Modified Eagle Medium) supplemented with 10% FBS (Gibco, 10099158).

Retina samples collection

Fetal eye samples were acquired from voluntarily donated aborted fetuses between gestational weeks 16 to 22. For 10x Genomics snATAC&GEX-Seq analysis, the ciliary margin zone and neural retina regions of the eye samples were meticulously dissected separately under a microscope and stored at -80°C for subsequent analysis. For Stereo-sequencing, the eye sample was snap-frozen in liquid nitrogen pre-chilled isopentane in Tissue-Tek OCT (Sakura, 4583) and then transferred to a -80℃ freezer for storage before the experiment. For immunocytochemistry and H&E staining, the samples were fixed in 4% paraformaldehyde (Beyotime, P0099) for 1 h, followed by gradient sedimentation using 10%, 20%, and 30% sucrose solutions (Beyotime, ST1672). Subsequently, they were embedded in NEG-50 (Thermo, 6502) and stored at -80°C for further processing. For cell isolation and culture, the samples were collected in ice-cold PBS (Gibco, c14190500cp), gently fragmented into small pieces, and then centrifuged at 200g for 2 min. The supernatant was removed, and 1 mL of digestion buffer (consisting of 2 mg/mL collagenase IV (Gibco, 17104019), 10 U/μL DNase I (NEB, 11284932001), and 1 mg/mL papain (Sigma, P4762) in PBS) was added. The tissues were incubated at 37°C for approximately 15–20 min, with pipetting every 5 min to aid in tissue digestion and obtain single cells. Finally, an equivalent volume of neutralization buffer (10% FBS in PBS) was added to halt the digestion process.

Human retinal organoid differentiation

Human retinal organoid differentiation was conducted following established protocols[34,68]. H9 hESCs were digested into single cells using TrypLE (Gibco, 12563-011) containing 0.05 mg/mL DNase I and 20 μM Y-27632. The cell concentration was adjusted to 120,000 cells/mL using Type I differentiation medium, which consisted of 45% IMDM (Thermo, 12440053), 45% F12 (Thermo, 11765054), 10% KSR

(Gibco, 10828010), 1% GlutaMAX (Thermo, 35050061), 450 μM Monothioglycero (Sigma, M6145), 1% Pen Strep (Gibco, 15140122) and 20 μM Y-27632. The cells were seeded into a low-adhesion V-bottom 96-well plate at a volume of 100 μL per well. On the 6th day of culture, half of the Type I differentiation medium was replaced with fresh medium containing 3 nM hBMP4 (R&D, 314-BP). This medium replacement was repeated on the 9th, 12th, and 15th days with fresh medium. On the 18th day, the cell aggregates were transferred to a 10 cm non-adherent culture dish, and the culture medium was switched to Type II differentiation medium. Type II medium consisted of 90% DMEM/F12-Glutamax medium (Thermo, 10565042), 10% FBS (Biological Industries, 04-001-1A), 1% N2, 0.1 mM Taurine (Sigma, T8691), 0.5 μM Retinoic acid (Sigma, R2625), and 1% Pen Strep. Long-term culture was maintained under high oxygen conditions (40% O_2), and the state and morphology of the organoids were continuously monitored in real-time using an inverted fluorescence microscope.

Fetal retina sample processing and single-cell multiomic sequencing

Preparation of Single-Cell Nuclear Suspension: Freshly frozen retina samples are selected for the preparation of single-cell nuclear suspensions through a series of steps, including cell membrane lysis, filtration, washing, and density gradient centrifugation or flow cytometry sorting. Subsequently, quality control tests are performed to assess nuclear integrity and concentration. It is required that the nuclear membrane remains intact, without noticeable impurities and fragments. Cell viability should be less than 5%, the aggregation rate should be less than 5%, nuclear concentration should fall within the range of 2000–3000 nuclei/μL, and the volume should exceed 60 μL. Wash the fetal retina samples twice with PBS, use digestion solution to digest at 37°C for 10 min to prepare single cells, and perform quality control tests for nuclear integrity and concentration. Single-Cell Sequencing: Following the manufacturer's instructions provided in the CG000338 Chromium NextGEM Single Cell Multiome ATAC_GEX (10x Genomics, PN-1000283) User Guide RevE, use the Chromium Controller to generate GEMs (Gel Bead-In-Emulsions) by combining the single-cell nucleus suspension/transposase with Gel Beads and oil droplets. Within the GEM oil droplets, the gel beads are lysed, and under PCR conditions, oligos containing Poly (dT) capture RNA, while oligos containing spacers capture transposed DNA sequences, both of which are labeled with 10x barcodes corresponding to the target sequences. Subsequently, the GEMs are broken, and the target fragments captured by magnetic beads are recovered. After pre-amplification, a 160 μL mixture is obtained, including complete DNA sequences with read1N and read2N, as well as amplified transcriptomic cDNA sequences. From the pre-amplification product, 40 μL is taken for ATAC library construction, directly adding a sample index for amplification. After purification, an ATAC library is obtained, which undergoes quality inspection. At the same time, 35 μL of the pre-amplification product is taken for cDNA amplification and purification. The purified cDNA undergoes fragmentation, end repair, A-tailing, adapter ligation, and dual-index amplification to complete library construction. The constructed library undergoes quality inspection, and Illumina NovaSeq 6000 sequencer is used to perform sequencing of the transcriptome using the PE150 sequencing strategy. The ATAC library is sequenced using the PE50 sequencing strategy.

Multiomic sequencing data processing and analysis

Single-cell multi-omic sequenced files were processed for demultiplexing and analyzed using Cell Ranger-ARC (v2.0.2). We used the human reference genome GRCh38 as reference to map genes. Single- nucleus RNA sequencing (snRNA-seq) data were analyzed using Seurat (v4.1.1)[59], and single- nucleus ATAC (snATAC-seq) data were analyzed using Signac (v1.9.0) [73]. For snATAC-seq data, calling peaks were used the MACS2 and the genomic positions were mapped and annotated with the reference human genome EnsDb.Hsapein.v86 and hg38. To obtain high-qualified cells, we adopted a stringent criterion to filter out low quality cells with < 1000 or > 20000 expressed gene counts, < 1000 or > 20000 fragment counts, > 0.05% blacklist fraction, < 2 transcription start site (TSS) enrichment, > 2% nucleosome signal, > 5% mitochondrial rate and > 10% ribosomal rate. Due to nuclei-derived samples indeed not contain valid cytoplasmic mitochondrial content; dead cells were excluded by removing cells with very low RNA yields.

Furthermore, we performed downstream analyses of data normalization, integration, and assay build. The “SCT” transform method was leveraged to process gene expression data, and the “RunTFIDF” and “RunSVD” function were used to process ATAC data. Integrating snRNA-seq and snATAC-seq data were conducted by anchoring using “FindIntegrationAchors”. Both methods of “rpca” and “SCT” normalization were used to dimensional reduction and batch correction for integrated snRNA-seq data, respectively. The “lsi” method was applied along with “RunTFIDF” and “RunSVD” for dimensional reduction and batch correction of integrated snATAC-seq data. Based on reductions from both gene expression and ATAC data, “FindMultimodalNeighbors” was utilized to obtain a joint neighbor graph, and “FindClusters” with SLM algorithm was utilized to identify cell clusters with the cluster resolution set to 0.5. The function of “FindMarkers” based on the Wilcoxon sum-rank test method was used to determine highly expressed genes, and “LR” test method was used to determine up-regulated motif accessibility. Based on differential feature analysis results, we annotated cell types in the integrated datasets by using well-known marker genes. The Uniform Manifold Approximation and Projection (UMAP) method was applied to visualize the integrated single-cell data distribution in two-dimensional space.

To calculate RNA velocity, we used both velocyto (v0.17.17) [74] and scVelo (v0.2.4) [50] to analyze reads that passed the quality control after clustering as instructed. First, the standard velocyto pipeline was run to count spliced and unspliced reads for each sample based on the filtered CellRanger-generated bam files. Then the output loom file was used as input for scVelo based on the dynamic model to estimate velocity embedding. We also applied the partition-based graph abstraction method (PAGA, v1.2)[52], a function of Scappy (v1.9.3) [75] python package, to infer the potential differential trajectory with default setting.

Stereo-sequencing and analysis

Tissue processing and *in situ* reverse transcription: Cryosections of the eye sample were cut at a thickness of 10 μm using a Leika CM1950 cryostat. The sections were attached to the surface of the Stereo-seq chip (BGI) and incubated at 37°C for 3 min. After that, the sections were fixed in methanol and

incubated at -20°C for 40 min before preparing the Stereo-seq library. The same sections were stained with a nucleic acid dye (Thermo, Q10212). After washed with 0.1x SSC buffer (Thermo, AM9770) supplemented with 0.05 U/mL RNase inhibitor (NEB, M0314L), the sections placed on the chip were permeabilized using 0.1% pepsin (Sigma, P7000) in 0.01 M HCl buffer, incubated at 37℃ for 5 min and then washed with 0.1x SSC buffer supplemented with 0.05 U/mL RNase inhibitor. RNA released from the permeabilized tissue and captured by the DNB was reverse transcribed overnight at 42℃ using SuperScript II (Invitrogen, 18064-014). After reverse transcription, tissue sections were washed twice with 0.1x SSC buffer and digested with Tissue Removal buffer at 55℃ for 10 min. cDNA-containing chips were then subjected to Prepare cDNA Release Mix treatment for overnight at 55℃. cDNA was purified using the VAHTSTM DNA Clean Beads (0.8×).

Library construction and sequencing: The resulting cDNAs were amplified with KAPA HiFi Hotstart Ready Mix (Roche, KK2602) with 0.8 mM cDNA-PCR primer. The concentrations of the resulting PCR products were quantified by QubitTM dsDNA Assay Kit (Thermo, Q32854). A total of 20 ng of DNA were then fragmented with in-house Tn5 transposase at 55℃ for 10 min, after which the reactions were stopped by the addition of 0.02% SDS and gently mixing at 37℃ for 5 min after fragmentation. Fragmented products were amplified as described below: 25 mL of fragmentation product, 1x KAPA HiFi Hotstart Ready Mix and 0.3 mM Stereo-seq-Library-F primer, 0.3 mM Stereo-seq-Library-R primer in a total volume of 100 mL with the addition of nuclease-free H2O. The reaction was then run as: 1 cycle of 95℃ 5 min, 13 cycles of 98℃ 20 seconds, 58℃ 20 seconds and 72℃ 30 seconds, and 1 cycle of 72℃ 5 min. PCR products were purified using the AMPure XP Beads (0.63 and 0.153), used for DNB generation and finally sequenced on MGI DNBSEQ-Tx sequencer.

Stereo-seq raw data processing: Fastq files were generated using a MGI DNBSEQ-Tx sequencer. CID and MID are contained in the read 1 (CID: 1–25 bp, MID: 26–35 bp) while the read 2 consist of the cDNA sequences. CID sequences on the first reads were first mapped to the designed coordinates of the in situ captured chip achieved from the first round of sequencing, allowing 1 base mismatch to correct for sequencing and PCR errors. Reads with MID containing either N bases or more than 2 bases with quality score lower than 10 were filtered out. CID and MID associated with each read were appended to each read header. Retained reads were then aligned to the reference genome GRCh38-3.0.0 using STAR (DOI: 10.1093/bioinformatics/bts635) and mapped reads with MAPQ > 10 were counted and annotated to their corresponding genes. UMI with the same CID and the same gene locus were collapsed, allowing 1 mismatch to correct for sequencing and PCR errors. Finally, this information was used to generate a CID-containing expression profile matrix. The whole procedure was integrated into a publicly available pipeline SAW available at https://github.com/BGIResearch/SAW.

Stereo-seq clustering and analysis: Expression profile matrix was divided into non-overlapping 26521 bins covering an area of 14650 x 18400 DNB. The resulting cells were further processed by Seurat (34062119) followed by SCTransform and scaling. 2000 feature genes were selected and top 20 principal components with the highest explained variance from the PCA results were selected to enhance our analysis. To classify the cell bins accurately and identify different cell types effectively, a resolution of 4

was chosen for clustering analysis in order to achieve precise results. Subsequently, clusters located in the CMZ region were isolated based on their spatial location and marker genes specific to this region. A re-clustering analysis was performed on this isolated CMZ region using a resolution of 1 and relying on marker genes defining RPE.stem-like cells and hNRSC. 'FindMarkers' function was also used to calculated the highly expressed genes for different clusters and celltypes. As for cells in other regions, annotation of all clusters was conducted based on their spatial location, different expression genes as well as known cell type markers obtained from single-cell data analysis. Finally, similar cell types were merged together after careful consideration.

Stereo-seq pseudotimes analysis: To infer the cell lineage of three interested cell types, namely hNRSC, RPCs, and PCs, we employed Slingshot (https://doi.org/10.1186/s12864-018-4772-0) for pseudotimes analysis. Slingshot stands out as an exceptionally robust and versatile tool that integrates stable techniques suitable for handling noisy single-cell data while effectively identifying multiple trajectories. It also applicability in Stereo-seq data scenarios. Furthermore, given the simplicity of the targeted cell populations and the presence of a solitary trajectory path, Slingshot enables swift inference of trajectories directly based on the original dimensionality-reduced data from Seurat. The technical support related to Stereo-seq in this study was provided by Annoroad Gene Technology (Beijing) Co., Ltd.

Organoid sample preparation and single-nucleus RNA sequencing

Following the manufacturer's guidelines for 10x Genomics single-nucleus RNA Sequencing, 5–10 hRO samples were chosen, and a series of steps were executed, including homogenization, cell membrane lysis, filtration, washing, and nuclear purification, with the aim of isolating single-cell nuclei. Subsequent to these procedures, quality control tests were conducted to assess nuclear integrity and concentration. The single-cell nuclei were then processed in accordance with the 10x Genomics Chromium Next GEM Single Cell3_v3.1_Rev_D (10x Genomics, PN-1000121) protocol for library construction and quality control. In brief, single nuclei were suspended in PBS containing 0.04% BSA. The nuclei suspension was loaded onto the Chromium Next GEM Chip G (10x Genomics, PN-1000120), and the Chromium Controller was utilized to create single-cell gel beads in the emulsion (GEMs) following the manufacturer's recommendations. Captured nuclei were lysed, and the resulting RNA was barcoded through reverse transcription within individual GEMs. This process generated barcoded, full-length cDNA, and libraries were subsequently constructed according to the manufacturer's protocol. Quality assessment of the libraries was conducted using Qubit 4.0 and the Agilent 2100, and sequencing was carried out on the Illumina NovaSeq 6000, aiming for a sequencing depth of at least 50,000 reads per nucleus with 150 bp (PE150) paired-end reads.

Single nucleus analysis

Raw single-nucleus RNA sequencing (snRNA-seq) data were processed by using the standard CellRanger pipeline to demultiplex and align sequencing output to the GRCh38 human reference genome. Quality control for organoids cells was performed using Seurat (v4.1.1)[59]. We filtered out low-quality cells with <

500 or > 5000 detectable genes, < 1000 expressed gene counts, > 2% mitochondrial rate, and > 3% ribosomal rate. The log normalizing and scaling for unique molecular identifier (UMI) counts was performed by the SCTransform function in Seurat package. FindVariableFeatures was performed using a variance-stabilizing transformation to identify the top 3000 highly-variable genes. Principal component analysis (PCA) was conducted to calculate principal components (PCs) that could explain most of the single-cell dataset through leveraging these highly variable genes. Batch effects among samples were removed by R package harmony (v0.1.0)[76] based on top 50 PCs. The shared nearest neighbor graph method was used to identify cell clusters with the resolution of 0.4. Similar with annotation of fetal eye, we assigned these clusters to organoid retinal cell types by using well-known specific marker genes. We used the UMAP method to visualize single-cell data distribution in two-dimensional space.

Developmental trajectory analysis

To infer the developmental trajectory, we applied both Monocle2 (v2.28.0)[77] and Monocle3 (v1.3.1)[51] to calculate the pseudotimes of cells from both fetal and hRO data snRNA-seq and snATAC-seq data, respectively. The standard protocol of Monocle2 and Monocle3 with default parameters was adopted to order cells into potentially differentiation trajectories, followed by optional statistical tests to find genes those alterations in expression over trajectories. The cell trajectories of Monocle2 were visualized for different cell types and different differentiation states, and the results of Monocle3 trajectory analysis were visualized in two-dimensional scatter plot. The pseudotime was calculated by setting hNRLCs at the root state.

Calculating the stemness scores of single cells

To evaluate the stemness of cells in lineage 1 for both fetal and hRO snRNA-seq data, we used the CytoTRACE (v0.3.3)[53] to estimate transcriptional diversity of each individual cell in terms of differential or stemness status. The cells in lineage 1 were given a stemness score ranging from 0 to 1 according to their differential potential. The higher score represents higher stemness and less differentiation, and the lower score represents lower stemness and more differentiation. Furthermore, we also leveraged an orthogonal method of Stem_ID/RaceID[54,78], an algorithm designed for discerning stem cells from all cell types, to validate the stemness of cells in lineage 1. By applying the “compentropy” function of the RaceID (v0.3.0) R package[78], we calculated the entropy of each cell from lineage 1 in both fetal and organoid data. Since entropy inversely correlates with cell differentiation state[79,80], thus, cells with high entropy indicate higher functional uncertainty and more differentiation potential (namely high stemness), while cells with low entropy indicate more differentiated states with constrained cell fates and functionalities (namely low stemness).

Regulon activity analysis

To assess the regulation intensity of transcription factors (TFs), we leveraged the workflow of single-cell regulatory network inference and clustering (pySCENIC v0.12.0) to calculate the activity of regulons based on the TFs and their target genes[56]. Following the standard pySCENIC protocol, we leveraged

GRNboost to identify potential genes that are co-expressed with TFs. To uncover putative direct-binding targets, RcisTarget was used to perform cis-regulatory motif analysis for each co-expression module. Only significant regulons were included for further analysis, and the activity of each regulon in each cell was estimated by the AUCell method. To connect regulons with cell types, we leveraged the Wilcoxon rank-sum test to prioritize cell type-specific regulons with the AUC scores. The AUC scores for each TF in each cell type were averaged for visualization of heatmap.

Inferring gene regulatory network based on single-cell multiomic sequencing data

We applied Pando (v1.0.5)[55] to fetal retinal data of multimodal single-cell measurements, where both RNA and ATAC components are measured in the same cell, to infer gene regulatory network (GRN). First, Pando selects candidate regions for GRN inference based on evolutionary conservation regions, prior cis-regulatory element regions, and data-driven accessible peaks from snATAC-seq data. Based on an extended motif database that obtains binding motifs and binding site predictions from JASPAR (2020 release)[81], CIS-BP database[82], and AnimalTFDB[83], Pando identifies putative cis-regulatory elements and putative trans-regulators (that is, TFs) of each gene. Subsequently, Pando uses a linear regression model to carry out the inference of the regulatory interactions between TF-binding site pairs and the target gene. To fit the linear regression model, the function glm from the stats R package using Gaussian noise was used. The fitted coefficients were examined for statistical significance using analysis of variance (ANOVA) to determine significant TF-motif-target triplets for pruning the network. To visualize the inferred TF network, the pairwise Pearson correlations of log-normalized expression of all TFs in the network across all cells were calculated. Based on the correlation value and fitted coefficients, Pando computes a combined TF-gene linkage score matrix and uses this matrix to perform principal component analysis (PCA). Top 20 PCs were used to generate the UMAP embedding of the TFs via the uwot R package with default parameters.

Jaccard similarity index

To evaluate the similarity of cell types between fetal retina and hROs, we applied the Jaccard similarity index to calculate the overlapped marker genes of the same cell type from snRNA-seq data between fetal retina and hROs. For a cell type t in both fetal and organoid retinal single-cell data, we used the "FindMarker" function in Seurat to calculate the significant up-regulated marker gene sets, which were donated as G_t^f and G_t^o for fetal and organoid, respectively. The top $n = \min\{|G_t^f|, |G_t^o|\}$ genes were selected to calculate the similarity, then the gene sets were represented as $G_{t,n}^f$ and $G_{t,n}^o$. Finally, the Jaccard index of cell type t was calculated as:

$$J_t = \frac{G_{t,n}^f \mathrm{I}\ G_{t,n}^o}{G_{t,n}^f \mathrm{U}\, G_{t,n}^o}$$

Immunocytochemistry and H&E staining

To prepare the organoids, they were fixed in 4% paraformaldehyde at 4℃ for 45 min. Subsequently, they were embedded in NEG-50 and cryosectioned at 14–16 μm thickness on slides using a Leica cryostat. The cryosections were then either utilized for immunocytochemistry or stored at -80°C for later use. Retina tissue samples were processed for cryosections using standard protocols. The procedure involved dissection of the retina tissue, followed by post fixation in 4% paraformaldehyde for 1 h. Gradient sedimentation is then performed with 10%, 20%, 30% sucrose solutions. The cryoprotected samples were then embedded in NEG-50 and cryosectioned at 16 μm thickness. Monolayer cells were fixed with 4% paraformaldehyde for 15 min to preserve their morphology. For immunocytochemistry, both the cryosections and monolayer cells were initially blocked and permeabilized in a solution containing 4% BSA (Beyotime, ST2254) and 0.5% Triton X-100 (Solarbio, T8200) for 1 h at room temperature. They were then incubated with primary antibodies overnight at 4°C. After primary antibody staining, the sections and cells were rinsed three times with PBS and subsequently incubated with secondary antibodies in the dark at room temperature for 1 h. Following the removal of the secondary antibody, the nuclei were stained with a 300 nM DAPI stainning solution (Thermo, D1306) for 15 min. Finally, the stained sections and cells were visualized using confocal microscopy (Leica). H&E staining of the sections was performed using the Hematoxylin and Eosin Staining Kit (Beyotime, C0105S). The stained sections were then scanned using the ZEN 2012 (blue edition) scanning system (Zeiss). Antibodies are described in Supplementary Table 4.

RNA-Seq and analysis

For each sample, total RNA was extracted using TRIzol reagent (Thermo, 15596018CN) and subsequently purified using the RNeasy Mini Kit (Qiagen, 74104), following the manufacturer's instructions. The quality

and quantity of the RNA were assessed using a NanoDrop 2000 spectrophotometer, Agilent 2100 Bioanalyzer, and Agilent RNA 6000 Nano Kit (Agilent, 5067 – 1511). Annoroad Gene Technology handled the RNA library construction and RNA sequencing. To create the sequencing libraries, the NEB Next Ultra RNA Library Prep Kit for Illumina (NEB, E7770L) was employed. Library clustering was carried out using the HiSeq PE Cluster Kit v4-cBot-HS (Illumina, PE-401-4001), following the manufacturer's recommendations. After cluster generation, the libraries were subjected to sequencing on an Illumina platform, generating 150 bp paired-end reads. The initial analysis of the data was performed utilizing BMKCloud, accessible at http://www.biocloud.net/[34].

Clonal sphere assay and induced differentiation

For the RSC clonal sphere assay, select the well-preserved and fresh samples; use a sterile V-Lance blade to separate the CMZ under a microscope. Prepare a digestion solution using 0.25% TE enzyme (with the addition of 50 μg/mL DNase and 20 μg/mL Y-27632). Digest the separated CMZ into single cells (digestion time ≤ 15 min). Resuspend the cells in serum-free (SFM) culture medium (48% DMEM (Gibco, C11995500bt), 48% F-12, 20 ng/mL bFGF (PeproTech, AF-100-18C), 20 ng/mL EGF (PeproTech, AF-100-15), 2% B27 (Gibco, 17504044), 1% N2 (Gibco, 17502048), 5 ng/mL heparin (Sigma, H3393) and 1% Pen Strep), and seed them in a pre-prepared 12-well culture plate. Perform a half-media change on day 3 and day 5, and incubate at 37°C in a carbon dioxide incubator for 7 days. After culturing the CMZ spheres for 7 days, transfer them to a 12-well plate treated with either poly-L-lysine or laminin. Use SFM culture medium containing 5% FBS for adherent culture. After 3 days of culture, the spheres will adhere to the bottom of the dish, and cells will start migrating out of the spheres. Then, transfer the spheres to retinal differentiation medium (88% DMEM/F12, 10% FBS, 0.5 μM RA, 20 ng/mL FGF2, 20 ng/mL EGF, 2 mM L-glutamine, 1% N2 and 1% Pen Strep) for differentiation culture. Change the medium every other day and continue differentiation culture until around day 20.

Establishment of the retinal organoid regeneration model

Select visually healthy and relatively mature hROs, aged over 60 days. Under a microscope, use a sterile V-Lance knife to excise the *VSX2*-tdTomato-labeled retinal portion, while preserving the rest of the organoid. Maintain the cultured organoids and establish a control group (simultaneous excision of the entire retina and ciliary margin). Utilize confocal microscopy for live-cell imaging to dynamically observe the regenerative repair process mediated by the CMZ-hNRSCs by tracking the *VSX2*-tdTomato-positive cells. Collect the organoid samples at critical time points of retinal regeneration for subsequent analysis.

EdU cell proliferation assay

Following the manufacturer's instructions, an appropriate amount of EdU (Beyotime, C0071S) was added to the culture medium and the organoids were incubated 24 h in a cell culture incubator. This allowed EdU to be taken up and integrated into newly synthesized DNA by actively proliferating cells within the organoid. After incubation, the cells were fixed in 4% paraformaldehyde at 4°C for 45 min to preserve their morphology. Next, the fixed organoids were embedded in NEG-50 and cryosectioned at 14–16 μm

thickness on slides using a Leica cryostat. The sections were then subjected to EdU staining using an EdU detection kit according to the provided instructions. Following EdU staining, the sections were further stained with DAPI for nuclear staining. Finally, the EdU-labeled cells were visualized and recorded using a fluorescence microscope.

10x Genomics visium spatial transcriptomic (ST) analysis

Staining and Imaging: The histological workflow utilized the Visium CytAssist Spatial Gene Expression kit (10x Genomics, PN-1000520) for Fresh Frozen tissues. Cryosections, measuring 10 μm in thickness, were cut and affixed onto GEX arrays. These sections were then placed on a Thermocycler Adaptor with the active surface and incubated at 37℃ for 5 min, followed by fixation in chilled methanol at -20℃ for 30 min. Subsequently, the sections were stained using H&E. Brightfield images were captured using a Leica DMI8 whole-slide scanner at 10x resolution.

Gene Expression and Transfer: Visium CytAssist Spatial Gene Expression analysis was performed using the Visium CytAssist Spatial Gene Expression for Fresh Frozen (FF) kits provided by 10x Genomics (PN-1000520). The tissue slices underwent crosslinking treatment, followed by probe hybridization and ligation on the crosslinked sections. Once successfully ligated, the probes, originally captured within the cells, were liberated through enzymatic digestion of RNA from the tissue sections using RNase, along with the tissue removal enzyme (10x Genomics, PN-3000387). Subsequently, the released probes were extended, eluted, and then transferred to new tubes for further analysis and utilization.

cDNA Library Preparation for Sequencing: The probe extension and library construction procedures followed the established Visium workflow for Fresh Frozen samples. Libraries underwent paired-end dual-indexing sequencing, and afterward, they were sequenced on an Illumina Novaseq6000 sequencer, with a targeted sequencing depth of at least 100,000 reads per spot. The sequencing strategy employed was paired-end 150 bp. CapitalBio Technology conducted this sequencing process.

Data Preprocessing and Quality Control: ST sequencing data were processed using the CellRanger V3 platform. Raw sequencing reads were aligned to the human genome (GRCh38, ENSEMBL). The Space Ranger output files were imported into Seurat (v4.1.1) for subsequent analysis. Raw data underwent quality control to filter out low-quality spots and genes (lowqspot = 0.01, mitper = 25, geneExprMin = 10). Gene expression values were then normalized using SCTransform to account for technical variability and to ensure accurate downstream analyses.

Dimensionality Reduction and Clustering: Normalized data were subjected to dimensionality reduction using Principal Component Analysis (PCA) through the RunPCA function. FindNeighbors and FindClusters (cluster_res = 0.6) functions were applied to yield clusters of spatial transcriptomic (ST) spots representing distinct cellular neighborhoods. To visually explore the spatial organization of ST spots, a Uniform Manifold Approximation and Projection (UMAP) was generated using the RunUMAP function. To uncover genes differentially expressed between spot clusters, the FindAllMarkers function was employed. DotPlot visualizations were generated to present the expression levels of these marker

genes across different spot clusters. Utilizing cell type-specific marker genes derived from single-cell data, each spot cluster was annotated with the corresponding cell types. In cases where multiple cell types shared the same spot cluster, these were denoted using a '/' delimiter.

SPOTlight Deconvolution: To map single-cell data onto spatial spots, we employed the SPOTlight method, which employed a deconvolution algorithm based on the differential expression marker genes from snRNA-seq data. The spotlight_deconvolution function calculated the proportional representation of distinct cell types within each spot. This information was then used to generate the SpatialFeaturePlot, illustrating the distribution of various single-cell cell types across the spatial landscape.

Cell Type Annotation and Pseudotemporal Analysis: For insights into pseudotime of ST spots, the spatial.trajectory.pseudotime method from the stlearn package was employed. The pl.gene_plot function, using the "CumSum" approach, depicted the expression level of single-cell marker genes for hNRSCs across spatial spots.

Flow cytometry

The samples underwent two washes with DPBS solution. Subsequently, 1.5 mL of a digestion solution, comprising 0.25% Trypsin-EDTA (Thermo, 25200056), 50 μg/mL DNase , and 20 μg/mL Y-27632, was added to the samples. They were then incubated in a 37°C cell culture incubator for 10–15 min. Once it was confirmed that the majority of the masses had visually disappeared, 3 mL of a neutralizing solution composed of 90% DPBS, 10% FBS, 50 μg/mL DNase , and 20 μg/mL Y-27632 was added to halt the reaction. Subsequently, the single cells resulting from trypsinization underwent multiple washes with 3%FBS. Afterward, they were stained with antibody in PEB buffer (PBS containing 0.5% BSA and 2 mM EDTA) for 30 min while kept on ice. Following staining, the cells were filtered through a 100 μm nylon mesh and subjected to fluorescence analysis using FACSCanto II (Becton Dickinson).

Subretinal transplantation

The transplantation therapy was performed on rd10 mice, a recognized model of retinal degeneration. All experiments conducted in this study followed the guidelines and permissions provided by the Institutional Committee of Laboratory Animal Ethics. A cell suspension (1×10^5 cells/μL) in a volume of 1-1.5 μL was injected into the subretinal space. Prior to the procedure, 2–4-week-old mice were anesthetized with an intraperitoneal injection of sodium pentobarbital (40 mg/kg, Sigma, P3761). To facilitate the procedure, the pupils were dilated using 1% tropicamide, followed by the application of topical anesthetic proparacaine hydrochloride (0.5%). Injections were carried out using a Hamilton syringe fitted with a 33-gauge needle under an operating microscope. Following the surgery, ofloxacin ointment (Sinqi Pharmaceutical, H10940177) was applied topically for 3 days to prevent dry eyes and infection. All mice, including sham-transplanted, are fed cyclosporine (Sangon, A600352) 24 h before transplantation until 2 weeks post-transplantation to mitigate immune rejection in the mice. The efficacy of the transplantation therapy was then assessed at the specified time points to evaluate its effectiveness.

Electroretinogram Recording

Corneal scotopic flash electroretinogram recordings were conducted on the eyes of rd10 mice from postoperative weeks 2 to 20. In brief, following a 12 h period of dark adaptation, the mice were anesthetized with an intraperitoneal injection of sodium pentobarbital. The pupils of the mice were dilated using 1% tropicamide. To prevent hypothermia, the animals were maintained at a body temperature of 37°C using a heating pad. Two active gold electrodes were positioned on each cornea to serve as the recording electrodes. Reference and ground electrodes were subcutaneously placed in the mid-frontal and tail areas of the head, respectively. The ERG parameters for photopic responses were set as follows: stimulation intensities at 0.48 log candela (cd)•s/m2 (light 3.0). The ERG parameters for scotopic responses were configured as follows: stimulation intensities at − 2.02 log cd•s/m2 (dark 0.01), 0.48 log cd•s/m2 (dark 3.0), and 0.98 log cd•s/m2 (dark 10.0).

Optomotor Response-based visual function assessment

To evaluate visual performance in each experimental group, we employed the optomotor response (qOMR) as a visual-driven behavioral task. The detection system creates a virtual stimulation environment using four screens, with the animal positioned on a platform at the center of the setup. The system tracks the movement of the animal's head in real-time relative to the presented visual stimulus and objectively quantifies the OMR results. We designed and implemented a virtual stimulation protocol that included spatial frequencies ranging from 0.05 to 0.5 cycles per degree (c/deg). Each spatial frequency was randomly presented for 60 seconds, moving at a speed of 12° per second. Clockwise and counter-clockwise head tracing responses were used to assess each eye's performance. The qOMR score is calculated as the ratio of concordant-to-discordant body/head movements in response to the moving gratings displayed on the screens surrounding the animal. A qOMR score of 1.0 served as a threshold for sensory perception: animals with qOMR scores below 1.0 were considered unable to perceive the specific spatial frequency being investigated.

Plasmids Design and Construct

The sgRNA plasmids were constructed by restriction cloning of protospacers downstream of a U6 promoter using BbsI cut site on px330 (Addgene, 68807) by standard protocol. For ligation, single-stranded DNAs were annealed with 4-bp overhangs on both ends of the double-stranded DNAs, with these overhangs acting as a substrate for T4 DNA ligase. Cloning backbones were digested with either BbsI-HF (NEB, R3539S); Ligation was carried out by adding 1 µL T4 DNA ligase (5 U/µL, Thermo, EL0011) to give a total ligation reaction volume of 10 µL. The oligonucleotide sequences used for plasmid construction in this study are listed in Supplementary Table 5.

The shRNA plasmids were constructed by restriction cloning of downstream of U6 promoter using AgeI and EcoRI cut sites on pLKO.1 - TRC cloning vector (Addgene, 10878) by standard protocol. For a typical reaction, DNA oligo was diluted to 100 µM with ddH2O and annealed in NEB 2.1 buffer and heated at 95°C for 2 min before slowly cooling to room temperature. Ligation was carried out by adding 1 µL T4

DNA ligase to give a total ligation reaction volume of 10 μL. The oligonucleotide sequences used for plasmid construction in this study are listed in Supplementary Table 5.

For constructed *VSX2*-tdTomato plasmid, the P2A-tdTomato DNA sequence was synthesized by GENEWIZ, and inserted in-frame into *VSX2* gene Exon 5 before the stop codon. The homology arm DNA sequence was obtained from genomic DNA of H9 ES cells with PCR (Vazyme, P520), gel purified with FastPure Gel DNA Extraction Mini Kit (Vazyme, DC301). Then infusion into HDR vector (Constructed by our lab), which cut by HindIII-HF (NEB, R3104V) and MfeI-HF (NEB, R3589V), together with P2A-tdTomato with the Uniclone One Step Seamless Cloning Kit (Genesand, SC612). The oligonucleotide sequences and vector sequence used for plasmid construction in this study are listed in Supplementary Table 5.

Lentiviral package and transfection protocol

For lentivirus packaging, HEK-293 cells were seeded at 2.5×10^6 cells per dish on 10 cm dishes in DMEM medium[62]. 24 h after seeding, 5 μg psPAX2 plasmid (Addgene, 12260), 2.5 μg pMD2.G plasmid (Addgene, 12259) and 5 μg shRNA plasmid were mixed and prepared with transfection reagent (Yeason, 40802ES08) following the recommended protocol from the vendor. 72 h after transfecting, lentivirus was collected following the recommended protocol, concentrated overnight using Universal Virus Concentration Kit (Beyotime, C2901S) and used within 2 days to transduce H9 hESCs without a freeze thaw cycle.

For electroporation, hESCs were dissociated into single cells using Accutase solution (Stem Cell Technologies). About 1×10^6 cells were resuspended in a nucleofector solution, prepared following the manufacturer's instructions. This solution was prepared by combining 82 μL of P3 primary cell solution with 18 μL of supplement 1 (Lonza, V4XP-3032). To this mixture, 5 μg of a plasmid mixture was added, which included 2.5 μg of sgRNA plasmid and 2.5 μg of the *VSX2*-tdTomato targeting vector. The cell-plasmid mixture was then transferred into a nucleofection cuvette (Lonza). The cells inside the nucleofection cuvette were nucleofected using program CA137 on the Nucleofector 4D (Lonza). Following nucleofection, the cells were gently transferred to Matrigel-coated plates containing TeSR-E8 medium supplemented with 10 μM Y-27632 and cultured in a 37°C, 5% CO_2 incubator. After electroporation, the cells were exposed to 2 μg/mL puromycin (Yeason, 60210ES25) for approximately 7 days. Subsequently, puromycin-resistant clones were selected and expanded for genotyping.

Genomic DNA extraction and genotype

Genomic DNA extraction of cells is subsequently performed using FastPure Blood/Cell/Tissue/Bacteria DNA Isolation Mini Kit (Vazyme, DC112). The targeted region from collected genomic DNA was amplified using PCR (Phanta Flash Master Mix, Vazyme, P520) and sequenced using a Sanger sequencing platform (GENEWIZ). The PCR included 200 ng of genomic DNA and 0.5 μL to 10 nM of forward and reverse primers in a final reaction volume of 40 μL. In the PCR, samples were incubated for 3 min at 95°C; 10 s at 95°C, 5 s at 65°C and 15 s at 72°C for 35 cycles, and 1 min at 72°C. After the first PCR step,

products were assessed on a 1.2% TAE gel; products were purified using FastPure Gel DNA Extraction Mini Kit (Vazyme, DC301).

Tissue RNA extraction, cDNA preparation, and quantitative real-time PCR

After lentivirus infection, the CMZ was collected by dissected and each was homogenized separately in a ball mill. The total RNA was extracted using FastPure Cell/Tissue Total RNA Isolation Kit V2 (Vazyme, RC112) according to the manufacturer's instructions. The RNAs were reverse-transcribed using HiScript III 1st Strand cDNA Synthesis Kit (+ gDNA wiper) (Vazyme, R312) to synthesize cDNA. qRT-PCR was performed on a CFX Manager Real-Time PCR system (Bio-Rad) using specific primers and Taq Pro Universal SYBR qPCR Master Mix (Vazyme, Q712). The results were calculated as ΔΔCT using GAPDH as internal reference transcript. ΔΔCT was calculated as ΔCT of the Knock down−ΔCT of the control. To work out the fold of gene expression, we performed 2-ΔΔCT. The primer sequences were provided in Supplementary Table 5.

Statistical analyses

All experiments were carried out autonomously and replicated a minimum of three times. The outcomes are expressed as the mean ± SD. For comparing two groups, an unpaired two-tailed Student's t-test was employed, whereas one-way ANOVA with Tukey's test or Dunnett's multiple comparisons test was utilized for contrasting multiple groups. Functional enrichment analyses were conducted to identify differential expression genes enriched GO-term biological processes using WebGestalt[84] and biological pathways using Metascape[85]. The statistical analysis was conducted using SPSS Statistics 19.0 software. Statistical significance was established for p values less than 0.05.

Declarations

Ethics statement

The current study involving donated human fetal eye samples received ethical approval from the Ethics Committee of the Eye Hospital of Wenzhou Medical University (Research License 2021-238-k-208-01). Informed consent forms were developed in adherence to the ISSCR guidelines for fetal tissue donation. All donors provided written informed consent and willingly contributed fetal eye samples after deciding to undergo legal pregnancy termination. None of the tissue samples used in this study had been previously involved in any procedures. All research procedures were carried out in accordance with the Regulations on the Management of Human Genetic Resources of the People's Republic of China.

Reporting summary

Further information on research design is available in the Nature Portfolio Reporting Summary linked to this article.

Data Availability

The RNA-Seq, snATAC&GEX-Seq and snRNA-Seq data are available at the Gene Expression Omnibus (GEO, NCBI) under accession number GSE242057. Source data are provided with this paper. Other data and material are available from the corresponding authors upon request.

Code availability

This paper does not report original code. All custom code used in this work is available upon request.

Acknowledgements

We thank Dr. Qingran Kong, Dr. Jiangfan Chen and Dr. Jinyi Zhang for constructive comments regarding this manuscript. We thank Dr. Zi-Bing Jin and Dr. Zhenhui Chen for technical assistance. This study was funded by the National Natural Science Foundation of China (82172882, 82101143), the Scientific Research Foundation for Talents of Wenzhou Medical University (QTJ18023 to JS), Zhejiang Provincial Natural Science Foundation of China (LR19C060001), and Wenzhou Medical University Basic Scientific Research Operating Expenses (KYYW202105).

Author contributions

J.S., J.Q., and K.Z. designed and supervised whole study; H.L., N.G., Q.Z., X.L., S.L., Y.Y., Q.R., H.H., Y.C., and M.C. performed the experiments; Y.M., Y.Z., G.L., C.D., and C.C. performed computational analysis; J.S. and J.Q. provided materials and funding support; H.L., Y.M., J.S., and K.Z. wrote the manuscript; All authors revised the manuscript.

Competing interests

The authors declare no competing interests.

References

1. Pfeiffer, R.L., Marc, R.E. & Jones, B.W. Persistent remodeling and neurodegeneration in late-stage retinal degeneration. *Prog. Retin. Eye Res.* **74**, 100771 (2020).
2. Choi, E.H. *et al.* In vivo base editing rescues cone photoreceptors in a mouse model of early-onset inherited retinal degeneration. *Nat. Commun.* **13**, 1830 (2022).
3. Voisin, A., Penaguin, A., Gaillard, A. & Leveziel, N. Stem cell therapy in retinal diseases. *Neural Regener. Res.* **18**, 1478-1485 (2023).
4. Canto-Soler, V., Flores-Bellver, M. & Vergara, M.N. Stem Cell Sources and Their Potential for the Treatment of Retinal Degenerations. *Invest. Ophthalmol. Vis. Sci.* **57**, ORSFd1-9 (2016).

5. Aladdad, A.M. & Kador, K.E. Adult Stem Cells, Tools for Repairing the Retina. *Curr. Ophthalmol. Rep.* **7**, 21-29 (2019).
6. Yoshii, C., Ueda, Y., Okamoto, M. & Araki, M. Neural retinal regeneration in the anuran amphibian Xenopus laevis post-metamorphosis: transdifferentiation of retinal pigmented epithelium regenerates the neural retina. *Dev.Biol.* **303**, 45-56 (2007).
7. Slavi, N. *et al.* CyclinD2-mediated regulation of neurogenic output from the retinal ciliary margin is perturbed in albinism. *Neuron* **111**, 49-64 e5 (2023).
8. Wan, Y. *et al.* The ciliary marginal zone of the zebrafish retina: clonal and time-lapse analysis of a continuously growing tissue. *Development* **143**, 1099-107 (2016).
9. Diacou, R. *et al.* Cell fate decisions, transcription factors and signaling during early retinal development. *Prog. Retin. Eye Res.* **91**, 101093 (2022).
10. Tsingos, E. *et al.* Retinal stem cells modulate proliferative parameters to coordinate post-embryonic morphogenesis in the eye of fish. *Elife* **8**(2019).
11. Shi, D., Tavhelidse, T., Thumberger, T., Wittbrodt, J. & Greb, T. Bifacial stem cell niches in fish and plants. *Curr. Opin. Genet. Dev.* **45**, 28-33 (2017).
12. Raymond, P.A., Barthel, L.K., Bernardos, R.L. & Perkowski, J.J. Molecular characterization of retinal stem cells and their niches in adult zebrafish. *BMC Dev. Biol.* **6**, 36 (2006).
13. Centanin, L. *et al.* Exclusive multipotency and preferential asymmetric divisions in post-embryonic neural stem cells of the fish retina. *Development* **141**, 3472-82 (2014).
14. Harris, W.A. & Perron, M. Molecular recapitulation: the growth of the vertebrate retina. *Int. J. Dev. Biol.* **42**, 299-304 (1998).
15. Reh, T.A. & Levine, E.M. Multipotential stem cells and progenitors in the vertebrate retina. *J.Neurobiol.* **36**, 206-20 (1998).
16. Fischer, A.J., Bosse, J.L. & El-Hodiri, H.M. The ciliary marginal zone (CMZ) in development and regeneration of the vertebrate eye. *Exp. Eye. Res.* **116**, 199-204 (2013).
17. Tang, X. *et al.* Bipotent progenitors as embryonic origin of retinal stem cells. *J. Cell. Biol.* **216**, 1833-1847 (2017).
18. Marcucci, F. *et al.* The Ciliary Margin Zone of the Mammalian Retina Generates Retinal Ganglion Cells. *Cell Rep.* **17**, 3153-3164 (2016).
19. Parain, K. *et al.* A large scale screen for neural stem cell markers in Xenopus retina. *Dev.Neurobiol.* **72**, 491-506 (2012).
20. Tropepe, V. *et al.* Retinal stem cells in the adult mammalian eye. *Science* **287**, 2032-6 (2000).
21. Coles, B.L. *et al.* Facile isolation and the characterization of human retinal stem cells. *Proc. Natl Acad. Sci.USA* **101**, 15772-7 (2004).
22. Coles, B.L., Horsford, D.J., McInnes, R.R. & van der Kooy, D. Loss of retinal progenitor cells leads to an increase in the retinal stem cell population in vivo. *Eur. J. Neurosci.* **23**, 75-82 (2006).

23. Cicero, S.A. *et al.* Cells previously identified as retinal stem cells are pigmented ciliary epithelial cells. *Proc. Natl Acad. Sci.USA* **106**, 6685-90 (2009).
24. Gualdoni, S. *et al.* Adult ciliary epithelial cells, previously identified as retinal stem cells with potential for retinal repair, fail to differentiate into new rod photoreceptors. *Stem Cells* **28**, 1048-59 (2010).
25. Belanger, M.C., Robert, B. & Cayouette, M. Msx1-Positive Progenitors in the Retinal Ciliary Margin Give Rise to Both Neural and Non-neural Progenies in Mammals. *Dev Cell.* **40**, 137-150 (2017).
26. Wahle, P. *et al.* Multimodal spatiotemporal phenotyping of human retinal organoid development. *Nat.Biotechnol.* (2023).
27. Hu, Y. *et al.* Dissecting the transcriptome landscape of the human fetal neural retina and retinal pigment epithelium by single-cell RNA-seq analysis. *PLoS Biol.* **17**, e3000365 (2019).
28. Wei, X. *et al.* Single-cell Stereo-seq reveals induced progenitor cells involved in axolotl brain regeneration. *Science* **377**, eabp9444 (2022).
29. Ma, Y. *et al.* Polygenic regression uncovers trait-relevant cellular contexts through pathway activation transformation of single-cell RNA sequencing data. *Cell Genom*.3, 100383 (2023).
30. Zhu, C., Preissl, S. & Ren, B. Single-cell multimodal omics: the power of many. *Nat. Methods* **17**, 11-14 (2020).
31. Nakano, T. *et al.* Self-formation of optic cups and storable stratified neural retina from human ESCs. *Cell Stem Cell* **10**, 771-785 (2012).
32. Cowan, C.S. *et al.* Cell Types of the Human Retina and Its Organoids at Single-Cell Resolution. *Cell* **182**, 1623-1640 e34 (2020).
33. Eldred, K.C. *et al.* Thyroid hormone signaling specifies cone subtypes in human retinal organoids. *Science* **362**(2018).
34. Liu, H. *et al.* Human embryonic stem cell-derived organoid retinoblastoma reveals a cancerous origin. *Proc. Natl Acad. Sci.USA* **117**, 33628-33638 (2020).
35. Xie, H. *et al.* Chromatin accessibility analysis reveals regulatory dynamics of developing human retina and hiPSC-derived retinal organoids. *Sci. Adv.* **6**, eaay5247 (2020).
36. Sridhar, A. *et al.* Single-Cell Transcriptomic Comparison of Human Fetal Retina, hPSC-Derived Retinal Organoids, and Long-Term Retinal Cultures. *Cell Rep.* **30**, 1644-1659 e4 (2020).
37. Sun, X. *et al.* One-stop assembly of adherent 3D retinal organoids from hiPSCs based on 3D-printed derived PDMS microwell platform. *Biofabrication* **15**(2023).
38. Kuwahara, A. *et al.* Generation of a ciliary margin-like stem cell niche from self-organizing human retinal tissue. *Nat. Commun.* **6**, 6286 (2015).
39. Voit, R.A. *et al.* A genetic disorder reveals a hematopoietic stem cell regulatory network co-opted in leukemia. *Nat. Immunol.* **24**, 69-83 (2023).
40. Lv, J. *et al.* Epigenetic landscape reveals MECOM as an endothelial lineage regulator. *Nat. Commun.* **14**, 2390 (2023).

41. Calvanese, V. *et al.* Mapping human haematopoietic stem cells from haemogenic endothelium to birth. *Nature* **604**, 534-540 (2022).
42. Mao, X. *et al.* Single-Cell RNA Sequencing of hESC-Derived 3D Retinal Organoids Reveals Novel Genes Regulating RPC Commitment in Early Human Retinogenesis. *Stem Cell Rep.* **13**, 747-760 (2019).
43. Wang, S., Poli, S., Liang, X. & Peng, G.H. Longitudinal single-cell RNA-seq of hESCs-derived retinal organoids. *Sci China Life Sci.* (2021).
44. Morizur, L. *et al.* Distinct Molecular Signatures of Quiescent and Activated Adult Neural Stem Cells Reveal Specific Interactions with Their Microenvironment. *Stem Cell Rep.* **11**, 565-577 (2018).
45. Kim, H. *et al.* Reelin function in neural stem cell biology. *Proc. Natl Acad. Sci.USA* **99**, 4020-4025 (2002).
46. Parameswaran, S., Xia, X., Hegde, G. & Ahmad, I. Hmga2 regulates self-renewal of retinal progenitors. *Development* **141**, 4087-97 (2014).
47. Dupacova, N., Antosova, B., Paces, J. & Kozmik, Z. Meis homeobox genes control progenitor competence in the retina. *Proc. Natl Acad. Sci.USA* **118**(2021).
48. Dulken, B.W., Leeman, D.S., Boutet, S.C., Hebestreit, K. & Brunet, A. Single-cell transcriptomic analysis defines heterogeneity and transcriptional dynamics in the adult neural stem cell lineage. *Cell Rep.* **18**, 777-790 (2017).
49. Lidgerwood, G.E. *et al.* Transcriptomic Profiling of Human Pluripotent Stem Cell-derived Retinal Pigment Epithelium over Time. *Genom Proteom Bioinf* **19**, 223-242 (2021).
50. Bergen, V., Lange, M., Peidli, S., Wolf, F.A. & Theis, F.J. Generalizing RNA velocity to transient cell states through dynamical modeling. *Nat. Biotechnol.* **38**, 1408-1414 (2020).
51. Cao, J. *et al.* The single-cell transcriptional landscape of mammalian organogenesis. *Nature* **566**, 496-502 (2019).
52. Wolf, F.A. *et al.* PAGA: graph abstraction reconciles clustering with trajectory inference through a topology preserving map of single cells. *Genome Biol.* **20**, 1-9 (2019).
53. Gulati, G.S. *et al.* Single-cell transcriptional diversity is a hallmark of developmental potential. *Science* **367**, 405-411 (2020).
54. Grün, D. *et al.* De novo prediction of stem cell identity using single-cell transcriptome data. *Cell stem cell* **19**, 266-277 (2016).
55. Fleck, J.S. *et al.* Inferring and perturbing cell fate regulomes in human brain organoids. *Nature*, 1-8 (2022).
56. Aibar, S. *et al.* SCENIC: single-cell regulatory network inference and clustering. *Nat. Methods* **14**, 1083-1086 (2017).
57. Cowan, C.S. *et al.* Cell types of the human retina and its organoids at single-cell resolution. *Cell* **182**, 1623-1640. e34 (2020).

58. Pham, D. *et al.* stLearn: integrating spatial location, tissue morphology and gene expression to find cell types, cell-cell interactions and spatial trajectories within undissociated tissues. *BioRxiv*, 2020.05. 31.125658 (2020).
59. Hao, Y. *et al.* Integrated analysis of multimodal single-cell data. *Cell* **184**, 3573-3587. e29 (2021).
60. Singh, M.S. *et al.* Retinal stem cell transplantation: Balancing safety and potential. *Prog. Retin. Eye Res.* **75**, 100779 (2020).
61. Liu, H. *et al.* Generation of an ESRG Pr-tdTomato reporter human embryonic stem cell line, CSUe011-A, using CRISPR/Cas9 editing. *Stem Cell Res.* **48**, 101983 (2020).
62. Li, S. *et al.* ESRG is critical to maintain the cell survival and self-renewal/pluripotency of hPSCs by collaborating with MCM2 to suppress p53 pathway. *Int.J.Biol.Sci.* **19**, 916 (2023).
63. Djojosubroto, M.W. & Arsenijevic, Y. Retinal stem cells: promising candidates for retina transplantation. *Cell Tissue Res.* **331**, 347-57 (2008).
64. Centanin, L., Hoeckendorf, B. & Wittbrodt, J. Fate restriction and multipotency in retinal stem cells. *Cell Stem Cell* **9**, 553-62 (2011).
65. Lamba, D., Karl, M. & Reh, T. Neural regeneration and cell replacement: a view from the eye. *Cell Stem Cell* **2**, 538-49 (2008).
66. Li, T. *et al.* Multipotent stem cells isolated from the adult mouse retina are capable of producing functional photoreceptor cells. *Cell Res.* **23**, 788-802 (2013).
67. Li, M. & Izpisua Belmonte, J.C. Organoids—preclinical models of human disease. *New Engl. J. Med.* **380**, 569-579 (2019).
68. Liu, H., Hua, Z.-Q. & Jin, Z.-B. Modeling human retinoblastoma using embryonic stem cell-derived retinal organoids. *STAR Protoc.* **2**, 100444 (2021).
69. Goyama, S. *et al.* Evi-1 is a critical regulator for hematopoietic stem cells and transformed leukemic cells. *Cell Stem Cell* **3**, 207-20 (2008).
70. Nagai, K. *et al.* Mecom mutation related to radioulnar synostosis with amegakaryocytic thrombocytopenia reduces HSPCs in mice. *Blood Adv.* (2023).
71. Terrell, D. & Comander, J. Current Stem-Cell Approaches for the Treatment of Inherited Retinal Degenerations. *Semin.Ophthalmol.* **34**, 287-292 (2019).
72. Wang, Y., Tang, Z. & Gu, P. Stem/progenitor cell-based transplantation for retinal degeneration: a review of clinical trials. *Cell Death Dis.* **11**, 793 (2020).
73. Stuart, T., Srivastava, A., Madad, S., Lareau, C.A. & Satija, R. Single-cell chromatin state analysis with Signac. *Nat. Methods* **18**, 1333-1341 (2021).
74. La Manno, G. *et al.* RNA velocity of single cells. *Nature* **560**, 494-498 (2018).
75. Wolf, F.A., Angerer, P. & Theis, F.J. SCANPY: large-scale single-cell gene expression data analysis. *Genome Biol.* **19**, 1-5 (2018).
76. Korsunsky, I. *et al.* Fast, sensitive and accurate integration of single-cell data with Harmony. *Nat. Methods* **16**, 1289-1296 (2019).

77. Qiu, X. *et al.* Reversed graph embedding resolves complex single-cell trajectories. *Nat. Methods* **14**, 979-982 (2017).
78. Grün, D. *et al.* Single-cell messenger RNA sequencing reveals rare intestinal cell types. *Nature* **525**, 251-255 (2015).
79. Guo, M., Bao, E.L., Wagner, M., Whitsett, J.A. & Xu, Y. SLICE: determining cell differentiation and lineage based on single cell entropy. *Nucleic Acids Res.* **45**, e54-e54 (2017).
80. Ma, Y. *et al.* Integration of human organoids single-cell transcriptomic profiles and human genetics repurposes critical cell type-specific drug targets for severe COVID-19. *Cell Prolif*. e13558 (2023)
81. Fornes, O. *et al.* JASPAR 2020: update of the open-access database of transcription factor binding profiles. *Nucleic Acids Res.* **48**, D87-D92 (2020).
82. Weirauch, M.T. *et al.* Determination and inference of eukaryotic transcription factor sequence specificity. *Cell* **158**, 1431-1443 (2014).
83. Hu, H. *et al.* AnimalTFDB 3.0: a comprehensive resource for annotation and prediction of animal transcription factors. *Nucleic Acids Res.* **47**, D33-D38 (2019).
84. Liao, Y., Wang, J., Jaehnig, E.J., Shi, Z. & Zhang, B. WebGestalt 2019: gene set analysis toolkit with revamped UIs and APIs. *Nucleic Acids Res.* **47**, W199-W205 (2019).
85. Zhou, Y. *et al.* Metascape provides a biologist-oriented resource for the analysis of systems-level datasets. *Nat. Commun.* **10**, 1523 (2019).

Figures

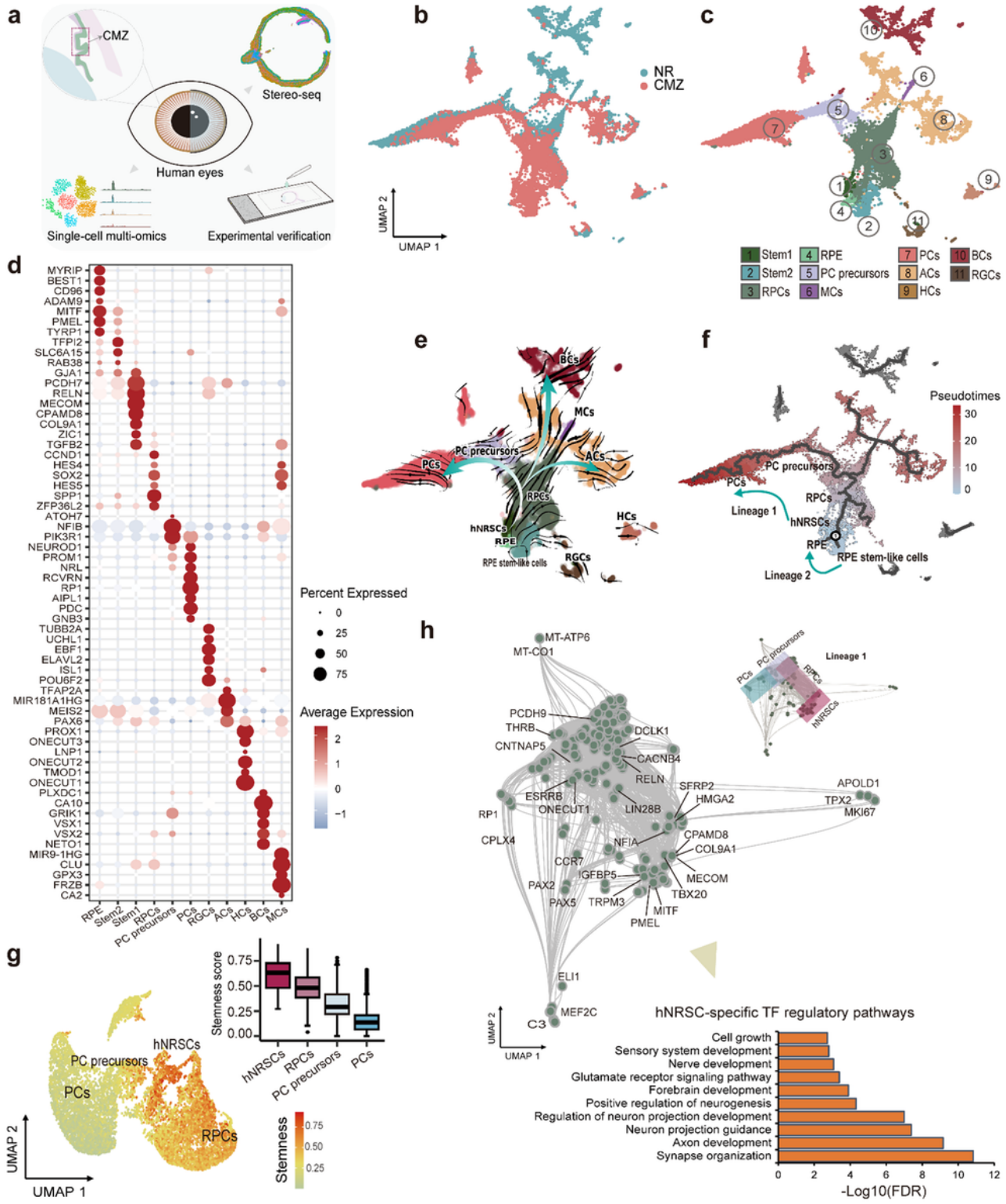

Figure 1

Identifying two stem-like cell subpopulations and their development lineages in CMZ of fetal retina at single cell level

a, Diagram illustrating the extraction of samples from both the CMZ and NR regions of the human fetal retina, followed by single-nucleus multi-omics sequencing (including ATAC and gene expression,

snATAC&GEX-Seq), along with Stereo-seq for spatial transcriptomics and subsequent experimental verification. CMZ: Ciliary Marginal Zone, NR: Neural Retina. **b**, Based on single-nucleus multi-omics data, UMAP visualization depicting cells from the CMZ and NR regions. Cells are color-coded based on their respective CMZ or NR regions. **c**, UMAP representation revealing identified cell types in both the CMZ and NR regions, determined by chromatin accessibility (ATAC) and gene expression (mRNA) data. RPC: retinal progenitor cell, RPE: retinal pigment epithelium cell, PC: photoreceptor cell, MC: Müller glial cell; AC: amacrine cell, HC: horizontal cell, BC: bipolar cell, RGC: retinal ganglion cell. **d**, Dot plot illustrating the expression of representative marker genes across various cell types in both regions. **e**, RNA velocity streamline plot illustrating the transitions of cell populations in the fetal retina using the scVelo method. The arrows represent a flow determined by the ratio of unspliced to spliced transcripts, predicting dynamic changes in cell identity. **f**, Pseudotime trajectory analysis of single-cell RNA profiling in cell types from both the CMZ and NR regions of the fetal retina, conducted through Monocle3. Cells are color-coded by pseudotimes, revealing two identified developmental lineages: lineage 1 includes hNRSCs-RPCs-PC precursors-PCs, and lineage 2 consists of RPE stem-like cells-RPEs. **g**, CytoTRACE analysis of cells in four cell types within lineage 1. In the lower left panel, UMAP visualization displays cells in lineage 1 colored according to the cytoTRACE-calculated stemness score. The upper right panel presents a boxplot illustrating stemness scores across the four cell types in lineage 1. **h**, UMAP representation of the inferred transcriptional factor (TF) network based on co-expression and inferred interactions between TFs and their targeted genes. Representative TFs and targeted genes are labeled in the gene regulatory network. The upper right panel shows a UMAP embedding shared by the four cell types in lineage 1, while the lower right panel displays a bar plot highlighting representative hNRSC-specific TF regulatory biological processes.

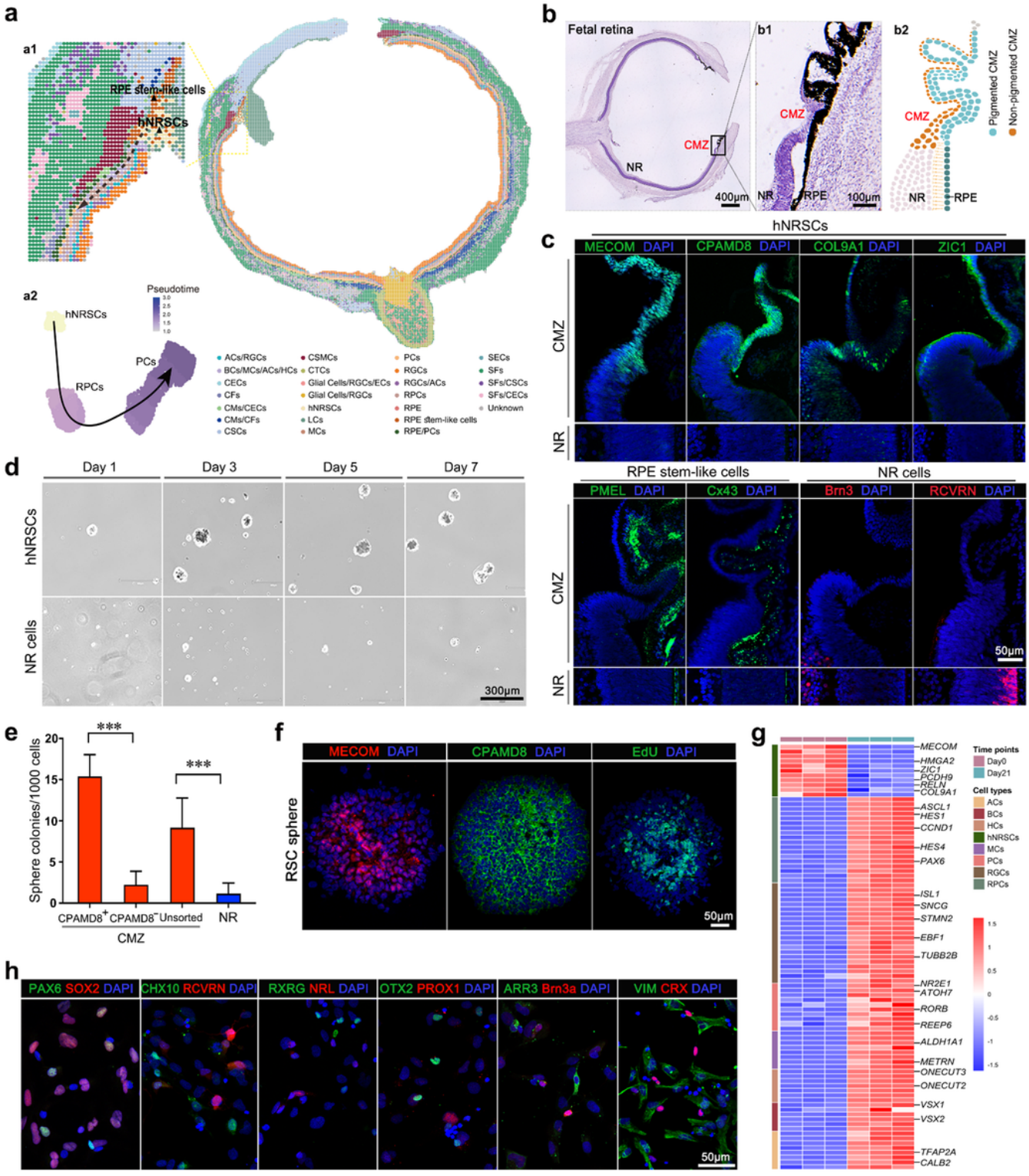

Figure 2

Characterization of hNRSCs in the CMZ of human fetal retina

a, Spatial visualization of cell types identified in the fetal retina using Stereo-seq. The dashed box highlights and magnifies the human CMZ of fetal retinas (a1). Pseudotime analysis of hRSLCs, RPCs, and PCs offers insights into the developmental progression of these cell types (a2). CECs: Corneal

Epithelial Cells, CFs: Choroidal Fibroblasts, CMs: Choroidal Melanocytes, CSCs: Corneal Stroma Cells, CSMCs: Ciliary Smooth Muscle Cells, CTCs: Connective Tissue Cells, ECs: Endothelial Cells, LCs: Lens Cells, SECs: Scleral Endothelial Cells, SFs: Scleral Fibroblasts. **b**, Representative Hematoxylin and Eosin (H&E) staining of the 18-week fetal retina, with a magnified view of the CMZ structure within the boxed region on the right (b1). (b2) Schematic illustration depicting the dual-layer architecture of the CMZ in the fetal retinas. **c**, Immunostaining demonstrates the expression of hNRSC representative signature genes, MECOM, CPAMD8, COL9A1 and ZIC1, along with representative markers PMEL and Cx43 for RPE and PRE stem-like cells, Brn3a for RGCs, and RCVRN for PCs in the CMZ and NR regions of 19-week fetal retinas. **d**, Representative micrographs of clonal spheres originating from hNRSCs and NR cells disassociated from fetal retinas (weeks 19-22). **e**, Quantitative analysis of sphere formation was performed on FACS-purified CPAMD8^{+} cells (hNRSCs), CPAMD8^{-} cells, and unsorted CMZ cells, which were isolated from the CMZ of fetal retinas (weeks 19-22). NR cells were used as the control. **f**, Immunostaining of hNRSC representative signatures MECOM and CPAMD8, along with proliferation marker EdU, in spheres derived from hNRSCs. **g**, Heatmap depicting expression patterns of hNRSC representative signature genes and the known retinal cell markers in spheres derived from hNRSCs, along with those which were induced to differentiate into retinal cells after three weeks. **h**, Immunostaining of cell type-specific proteins in retinal cells differentiated from hNRSCs. All representative examples of the data from at least three independent experiments are shown. Data are presented as mean ± SD; ***$P <$ 0.001.

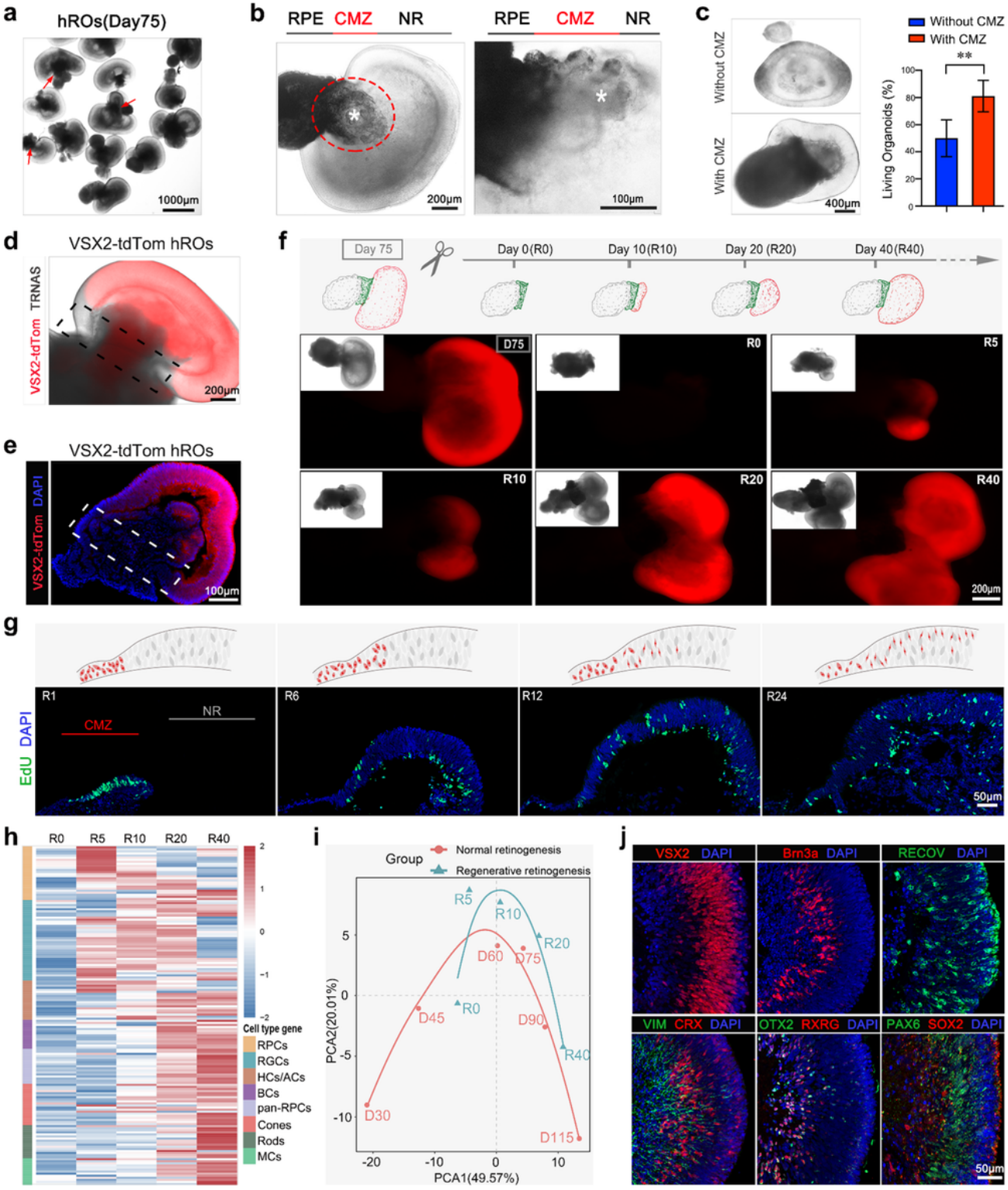

Figure 3

CMZ-like structures facilitate retinal regeneration in hROs

a, Representative bright-field image of 75-day-old hROs. Arrows indicate the putative CMZ-like structure. **b**, Illustrative micrographs of CMZ structures in hROs, highlighted by red circle, with asterisks denoting stem cell niche-like formations. **c**, Morphological images of hROs (Day 75) with and without the CMZ (left), and

survival count analysis of hROs with and without CMZ following an additional 40 days of cultivation (right). **d**, Representative image of 75-day-old hROs drived from *VSX2* (RPC marker)-tdTomato reporter hESC line, NR region is labeled with *VSX2*-tdTomato. Dashed-line box indicates the CMZ region. **e**, Fluorescence microscopy observation of the expression pattern of the *VSX2*-tdTomato in the NR region of the hRO sections. Dashed-line box indicates the CMZ region. **f**, Schematic illustration of the regeneration process of surgically excised NR structure by CMZ cells within hROs (upper panel); temporal monitoring of NR regeneration mediated by CMZ cells at key time points (Regenerative stage day 0, 5, 10, 20, 40; R0, R10, R20, R40) through tracking of regenerated *VSX2*-tdTomato positive RPCs within hROs (lower panel). (Insets) Bright-field images corresponding to the fluorescent images of hROs. **g**, Spatial distribution of EdU-labeled cells in hROs across different regeneration time points (lower panel). CMZ cells were labeled at the onset of regeneration (on developmental stage day 75) through a 24h exposure to EdU. Schematic depiction showing the progression of labeled dividing cells from the CMZ towards the NR central region as the process of regeneration unfolds (upper panel). **h**, The RNA-Seq results depict retinogenesis at different regenerative stages (R0, R5, R10, R20, R40) within hROs. **i**, Principal component analysis (PCA) of hROs across various regenerative and developmental stages reveals conserved retinogenesis between development and regeneration. **j**, Immunostaining of retinal cell type-specific proteins in hROs at regenerative day 40. All representative examples of the data from at least three independent experiments are shown. Data are mean ± SD; $^{**}P < 0.01$.

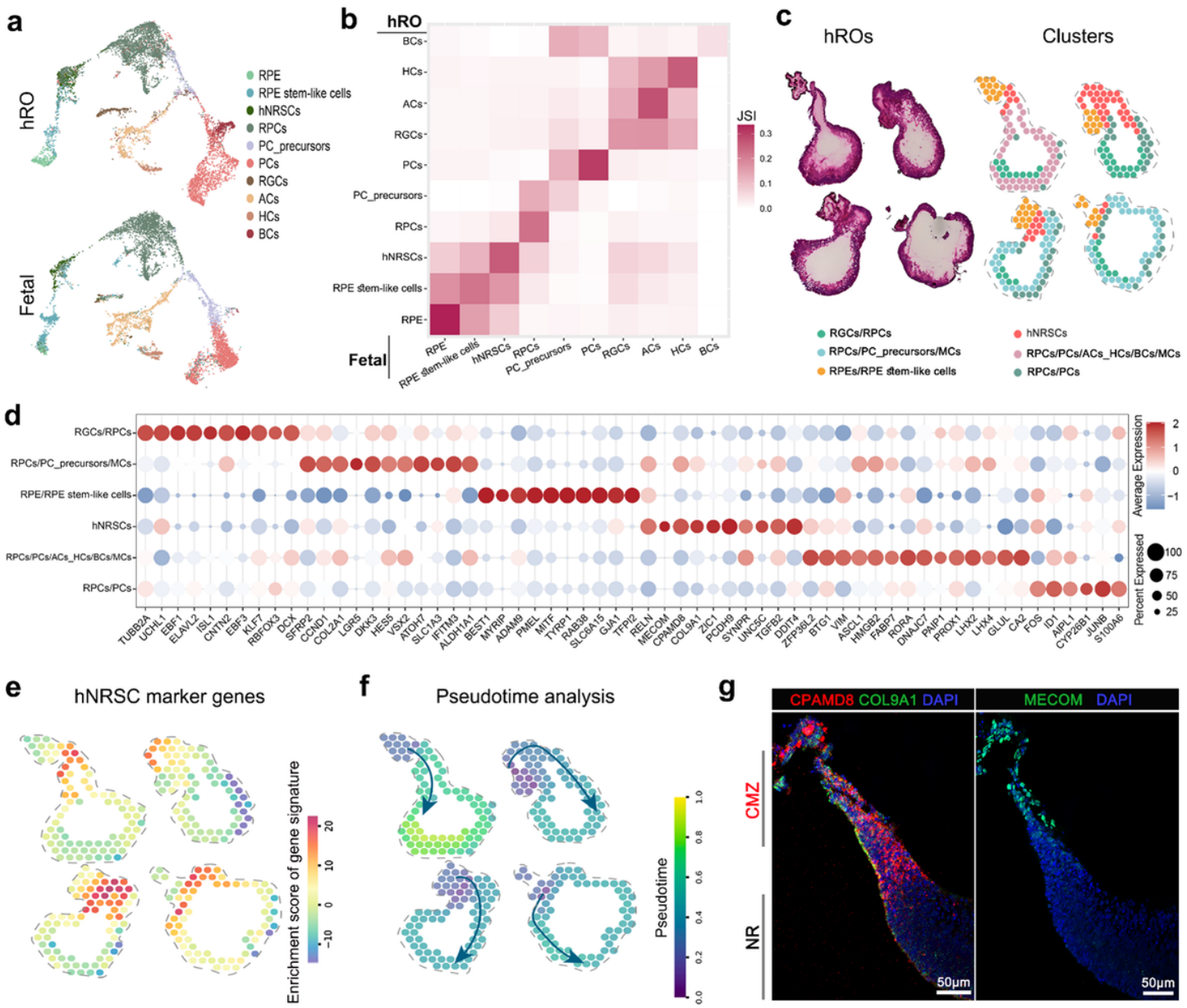

Figure 4

Presence of hNRSCs in hROs exhibiting high similarity to fetal hNRSCs

a, UMAP visualization of the consistence of cell types between hROs in 75 days (upper panel) and fetal retinas (lower panel). **b**, Heatmap showing the similarity of highly specific expressed genes in corresponding cell types between hROs and fetal retinas. The Jaccard similarity index (JSI) was used to measure the similarity. **c**, Spatial transcriptomics data of four representative hROs annotated with hROs-associated spot clusters. Hematoxylin and eosin (H&E) staining of hROs (left). Localization of spot clusters in the four hROs (right). The symbol (/) indicates potential presence of diverse cell types within the annotated clusters, reflecting the possibility of multiple cell co-occurrences within each spot. **d**, Dot plot showing expression of selected marker genes for the spot subsets from (**c**). **e**, Localization of hNRSCs-derived cell signatures differential expression gene markers from snRNA-seq in hROs. The localization depicts the distribution and spatial arrangement of distinct cell populations originating from

hNRSCs within the hROs. **f**, Pseudotime analysis mapping in the spatial location showing predicted lineages (hNRSCs-RPCs-PC precursors-PCs) within the hROs clusters. **g**, Immunostaining for hNRSC signature genes, CPAMD8, COL9A1 and MECOM, in hROs at day 75.

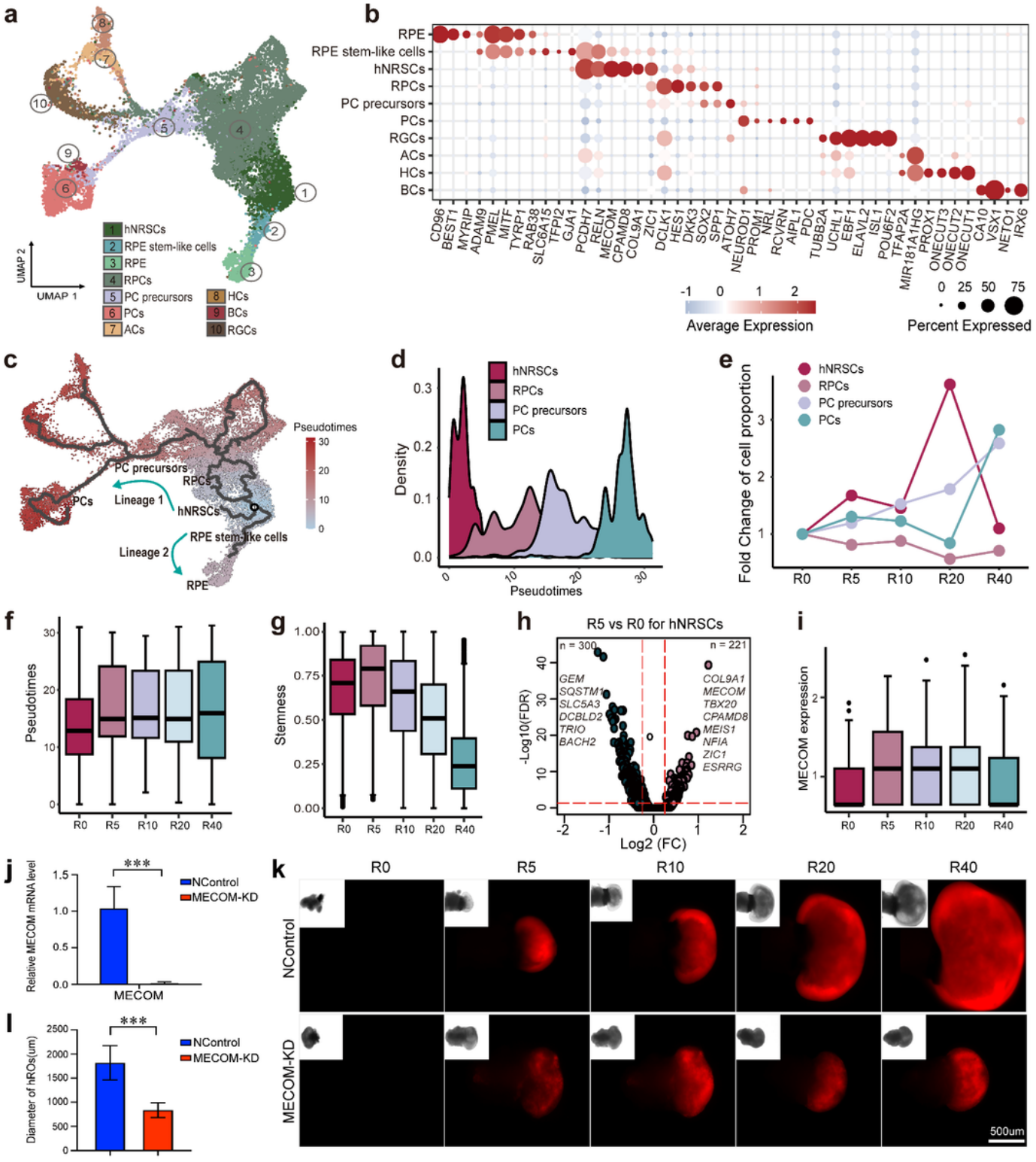

Figure 5

Putative cell lineage transition of human retinal organoid regeneration

a, UMAP plot showing 10 annotated cell types across five time points (day 0, day 5, day 10, day 20, and day 40) of hRO regeneration. **b**, Dot plot demonstrating expression of selected marker genes across cell types in hROs. **c**, Pseudotime trajectory analysis of cell types in snRNA-seq data on hRO regeneration via Monocle 3. Cells are colored by pesudotimes. (**d**) Density plot of the pesudotimes of four cell types (hNRSCs, RPCs, PC precursors, and PCs) in lineage 1. **e**, Line graph showing the fold change of proportion of cell types in lineage 1 across four regeneration time points (day 5, day 10, day 20, and day 40) compared to the initial time point (day 0). **f**, Correlation between the pseudotimes of cells and five time points of hRO regeneration. **g**, Boxplot showing the cytoTRACE-calculated stemness scores of cells in 10 cell types across five time points of hRO regeneration. **h**, Volcano plot showing the significantly differential expressed genes in hNRSCs at the time point of day 5 compared to the time point of day 0. Both the Wilcoxon test and log-transformed fold change log2 FC was used to calculate the significance of up-regulated and down-regulated genes. **i**, Boxplot demonstrating the expression of *MECOM* in cells from 10 maim cell types across five time points of hRO regeneration. **j**, Quantitative qPCR analysis of *MECOM* RNA levels at Day 10 after *MECOM* knockdown. n = 3. **k**, Representative micrographs depicting hROs at distinct regenerative time points (R0, R5, R10, R20, R40) following *MECOM* knockdown. The red fluorescence highlights the expression of *VSX2*-tdTomato within RPCs of the regenerated hROs. The insets display bright-field images of the regenerated hROs. **l**, Statistical analysis of the impact of *MECOM* knockdown on the size of regenerated hROs. n = 5. All representative examples of the data from at least three independent experiments are shown. Data are mean ± SD; $*P < 0.05$, $**P < 0.01$ and $***P < 0.001$.

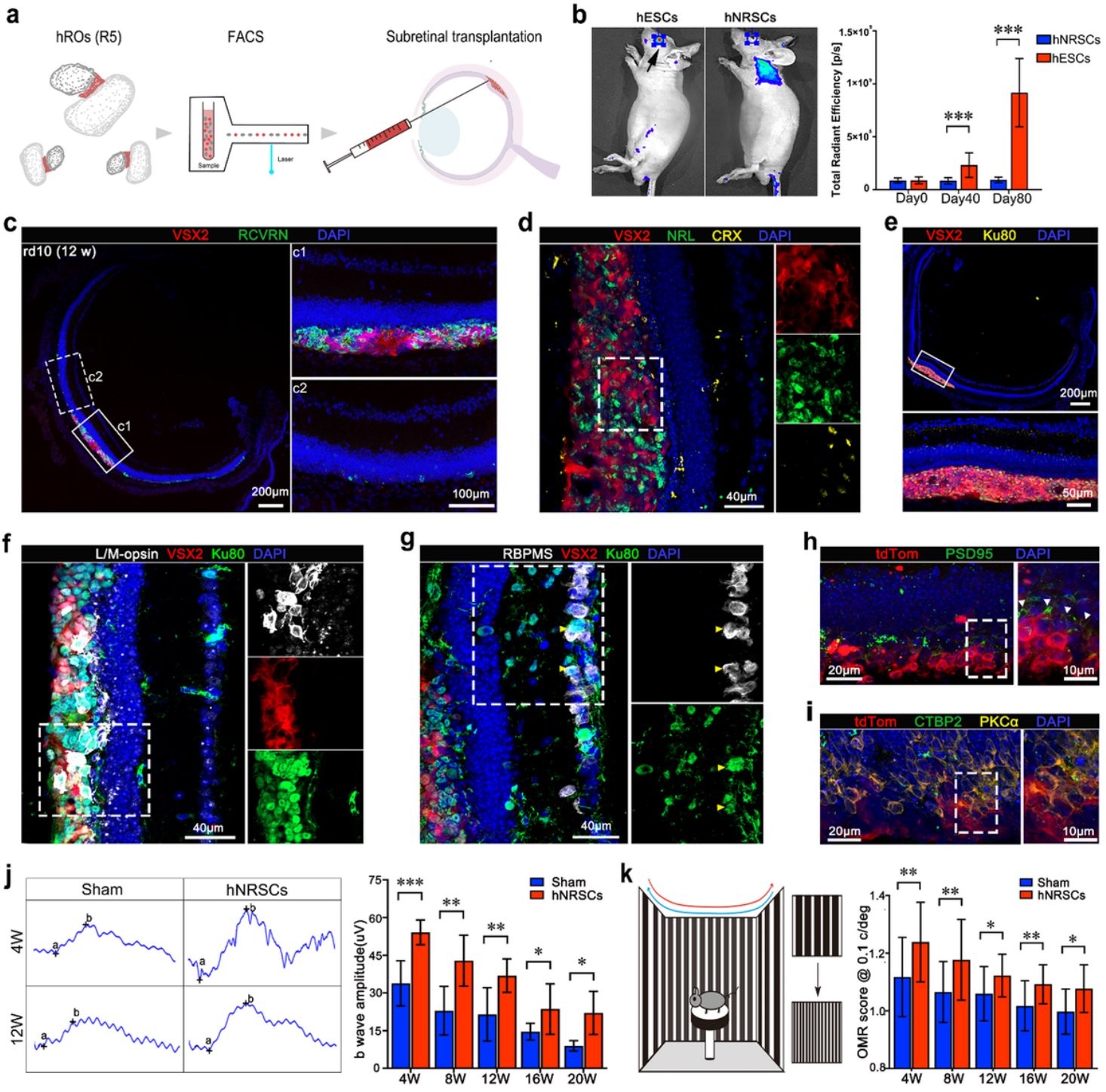

Figure 6

In vivo functional retinal repair via transplantation of hNRSCs derived from hROs

a, Schematic representation of the subretinal transplantation procedure for hNRSCs isolated through FACS from hROs into mice with RD disease. **b**, Representative *in vivo* imaging photographs showing tumor formation in nude mice after subretinal transplantation of H9 hESCs labeled with tdTomato. Nude mice exhibited pronounced tumor development 10 weeks post-transplantation with H9 hESCs, in contrast to the absence of tumor formation in mice transplantation with hNRSCs (right). Quantitative analysis

data are displayed in the right panel (n = 10 for each cell type). **c**, Immunostaining analysis of whole retinal sections reveals engrafted cells expressing the photoreceptor-specific marker RCVRN, leading to a noticeable increase in the thickness of the outer nuclear layer in contrast to non-transplanted regions. Magnified views of the area delineated by the solid-line box (c1) represent the transplanted region, as illustrated in the right panel, whereas regions enclosed by dashed-line box (c2) correspond to non-transplanted areas. **d**, Immunostaining analysis reveals the expression of early photoreceptor markers NRL and CRX in subretinal hNRSC transplants in retinal degeneration mice 10 weeks post-transplantation. Magnified views of the boxed regions are shown in the corresponding panel on the right. **e**, Representative Immunostaining analyses showing tdTomato-positive engraftment co-stained with the Ku80 human-specific marker, confirming its human origin. Magnified views of the boxed regions are shown in the bottom row. **f**, Immunostaining analysis reveals the expression of late photoreceptor marker L/M-opsin in subretinal hNRSC transplants in retinal degeneration mice 20 weeks post-transplantation, and these cells are all co-stained with Ku80. **g**, Immunostaining analysis shows that some transplanted cells migrate and integrate into the inner nuclear layer of the retina 20 weeks post-transplantation, expressing the RGCs marker RBPMS. Yellow arrows indicate $Ku80^+$ transplanted cells coexpressing RBPMS. **h**, Immunostaining analysis showing $tdTomato^+$ cell engraftment near the host retina, displaying expression of the synaptic connectivity protein PSD95. **i**, $tdTomato^+$ photoreceptor terminals in direct physical contact with synaptic protein CTBP-2 and situated near bipolar cells displaying PKCα staining. **j**, Representative b-wave responses of the hNRSC- and sham-transplanted groups were assessed through fERG at an intensity of 0.48 log ($cd*s/m^2$) (left). These responses were recorded sequentially in each eye at 4w, 8w, 12w, 16w and 20w post transplantation. Statistical analysis of b-wave amplitudes in the hNRSC- and sham-transplanted groups (right), n = 10 for each group. **k**, Schematic illustration of the optokinetic response test setup (left). Quantitative evaluation of visual acuity in the hNRSC- and sham-transplanted groups, obtained through the optokinetic response test at 4w, 8w, 12w, 16w and 20w post transplantation (right). n = 20 for each group. All representative examples of the data from at least three independent experiments are shown. Data are mean ± SD; $*P < 0.05$, $**P < 0.01$ and $***P < 0.001$.

Supplementary Files

This is a list of supplementary files associated with this preprint. Click to download.

- SupplementaryTable1.xlsx
- SupplementaryTable2.xlsx
- SupplementaryTable3.xlsx
- SupplementaryTable4.xlsx
- SupplementaryTable5.xlsx
- ExtendedDataFigures.docx